CAMBRIDGE
UNIVERSITY PRESS

Article

Crystal chemistry and miscibility of chernovite-(Y), xenotime-(Y), gasparite-(Ce) and monazite-(Ce) from Mt. Cervandone, Western Alps, Italy

Francesco Pagliaro[1]* , Paolo Lotti[1] , Alessandro Guastoni[2], Nicola Rotiroti[1], Tommaso Battiston[1] and G. Diego Gatta[1]

[1]Dipartimento di Scienze della Terra, Università degli Studi di Milano, Via Botticelli 23–20133 Milano, Italy; and [2]Dipartimento di Geoscienze, Università degli Studi di Padova, via Gradenigo 6–35137 Padova, Italy

Abstract

The crystal chemistry and crystal structure of the rare earth element phosphates, monazite-(Ce), $Ce(PO_4)$, and xenotime-(Y), $Y(PO_4)$, as well as the arsenates, gasparite-(Ce), $Ce(AsO_4)$, and chernovite-(Y), $Y(AsO_4)$, from the hydrothermal quartz-bearing fissures, related to pegmatites overprinted by amphibolite facies, cropping out at Mt. Cervandone, Western Alps, Piedmont, Italy, have been investigated by means of electron microprobe analysis in wavelength dispersion mode and single-crystal X-ray diffraction. The chemical data reveal the occurrence of a full solid solution among the isostructural chernovite-(Y) and xenotime-(Y) with tetragonal symmetry, whereas a wide miscibility gap is observed for the isostructural gasparite-(Ce) and monazite-(Ce) of Mt. Cervandone, with monoclinic symmetry. A significant chemical heterogeneity has been observed for several investigated samples, especially related to the Th content, which is locally enriched in $ThSiO_4$ grains. The analysis of the refined structural models demonstrates the significant control played by the composition of the tetrahedrally-coordinated (As,P)-bearing sites on the bulk unit-cell volume, and on the size and shape of the (REE)-coordination polyhedra.

Introduction

According to the IUPAC definition (Connelly *et al.*, 2005), the rare earth elements (REE) consist of a group of 17 elements, comprising the lanthanides (La–Lu or 'Ln series'), Y and Sc, characterised by a similar geochemical behaviour. REE are conventionally divided into light REE (LREE) and heavy REE (HREE) based on their atomic number. However, there are some complications and several authors have provided different thresholds to separate the two groups (Zepf, 2013). An elegant classification system has been provided by U.S. Geological Survey (2011), based on the electronic configuration of the $4f$ electron shell: LREE (Ce–Gd) are characterised by unpaired $4f$ electrons, whereas HREE (Tb–Lu) show paired electrons in the $4f$ shell; in addition, Y was included as one of the HREE (U.S. Geological Survey, 2011), as its atomic radius is intermediate between those of Ho and Er. REE are used in several applications, including permanent magnets, phosphors, catalytic converters, or as additives in glass and metal

alloys. Their mining exploitation is concentrated largely in China (U.S. Geological Survey, 2021) and their commodities export policy has changed significantly in the last decade, with the introduction of export quotas and taxes (Mancheri, 2015). For their elevated supply risk, all the REE have been classified as 'critical raw materials' by the European Commission (Blengini *et al.*, 2020). Major REE resources are hosted by carbonatites and other alkaline igneous rocks, pegmatites, iron oxide copper–gold deposits, skarn deposits and placers (Balaram, 2019). Hydrothermal alteration of granites and the related pegmatites, as well as the connected mobilisation and concentration of REE minerals, is a phenomenon of which the importance has been reported by several authors (e.g. Andersson, 2019; Cheng *et al.*, 2018; Migdisov *et al.*, 2019). Along with the carbonate bastnäsite $(Ce(CO_3)F)$ and common phosphates, i.e. monazite-(Ce) and xenotime-(Y), which are important REE ore minerals (Voncken, 2016), the isostructural arsenates gasparite-(Ce) and chernovite-(Y) have gained increasing attention (e.g. Cabella *et al.*, 1999; Mancini, 2000; Anthony *et al.*, 2000; Kolitsch and Holtsam 2004a; Ondrejka *et al.*, 2007; Breiter *et al.*, 2009; Mills *et al.*, 2010; Förster *et al.*, 2011; Kerbey, 2013; Papoutsa and Pe-Piper, 2014; Vereshchagin *et al.*, 2019). The aforementioned phosphates and arsenates belong to

*Author for correspondence: Francesco Pagliaro, Email: francesco.pagliaro@unimi.it
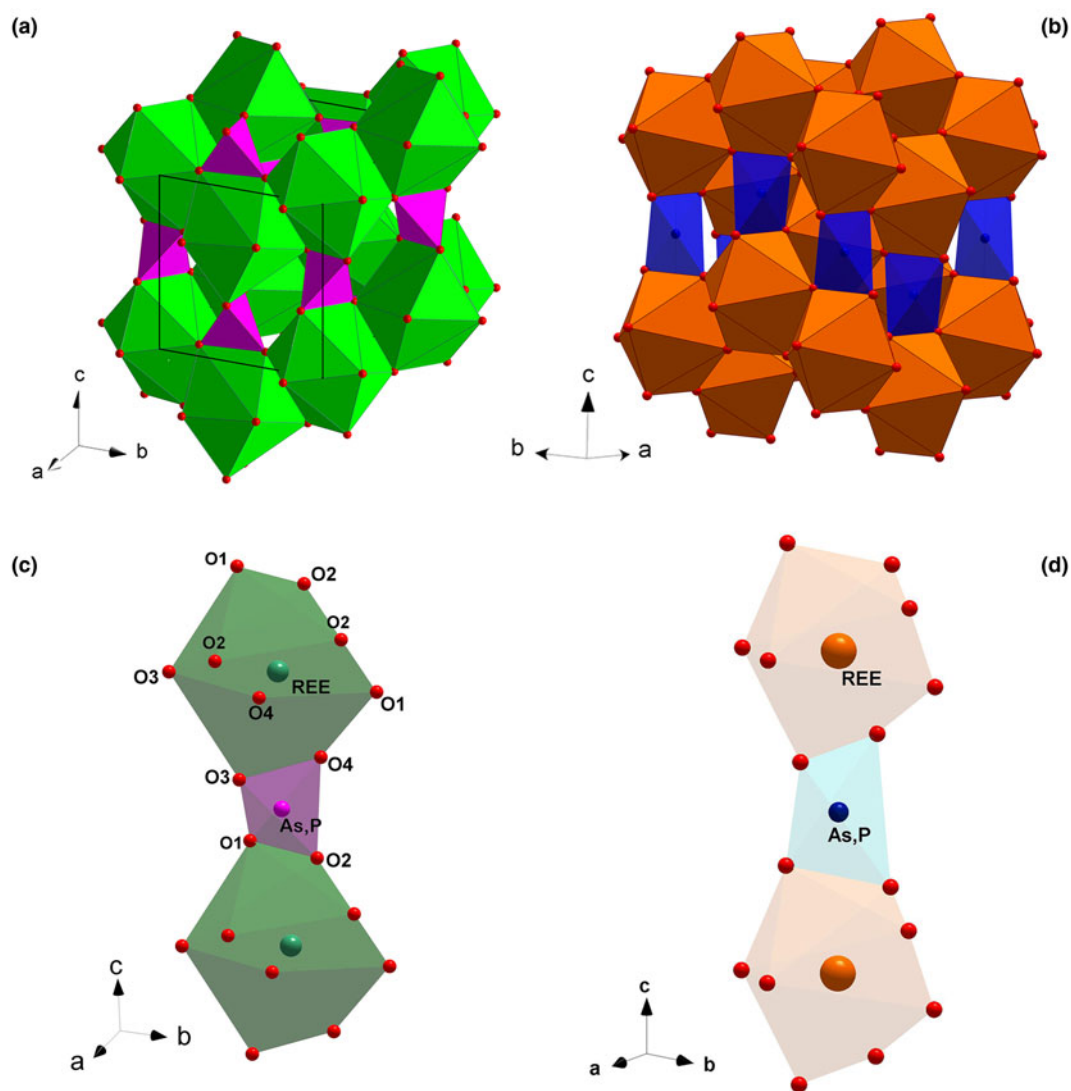
Fig. 1. The monazite-type (a) and the zircon-type crystal structures (b); (REE)-polyhedra and (P,As)-tetrahedra making the chains parallel to [001] in the monazite-type (c) and zircon-type structures (d).

the large family of ATO_4 minerals, where A stands for REE, Ca, U and Th, and T stands for tetrahedrally-coordinated cations (As, P and minor Si). The crystal structure of these minerals has been the subject of a large number of studies and reviews (e.g. Mooney, 1948; Boatner, 2002; Ni et al., 1995; Kolitsch and Holtsam, 2004b; Clavier et al., 2011). These ATO_4 compounds show two possible structural arrangements (Fig. 1): a monoclinic monazite-type structure (Fig. 1a) and a tetragonal zircon-type (also known as 'xenotime-type') structure (Fig. 1b). Chernovite-(Y), the zircon-type structured HREE-bearing arsenate, is a rare mineral; its crystal structure was first solved from the synthetic counterpart $YAsO_4$ (Strada and Schwendimann, 1934). The mineral chernovite-(Y) was first described from the Nyarta-Sya-Yu River, Urals (Goldin et al., 1967), and later found at the Mt. Cervandone mineral deposit in the Western Alps, Italy, as a solid solution between chernovite-(Y) and xenotime-(Y) (Graeser et al., 1973). Chernovite-(Y) has been recovered as an accessory mineral in hydrothermal environments, commonly found as an alteration product of minerals within A-type granites and gneisses (Breiter et al., 2009, Förster et al., 2011, Papoutsa and Pe-Piper, 2014, Li et al., 2019) and within reduction spots in slates by Kerbey (2013). Microcrystalline $YAsO_4$, along

with $LaAsO_4$ (i.e. gasparite-(La)), were also detected within the Fe–Mn deposits of the Corsaglia Valley, Maritime Alps, Italy (Cabella et al., 1999). In addition Mills et al. (2010) reported the presence of chernovite-(Y) along with arsenoflorencite-(La) in Mn-rich nodules from the Grubependity Lake cirque, Komi Republic, Urals.

The As-bearing analogue of monazite, a monoclinic arsenate, was also first described on the basis of the synthetic counterpart by Beall et al. (1981). It was first described in nature as gasparite-(Ce) by Graeser and Schwander (1987) and more recently also found as gasparite-(La) by Vereshchagin et al. (2019). A solid solution between monazite-(Ce) and gasparite-(Ce) has been found to occur at the Kesebol Mn–Fe–Cu deposit, Västra Götaland, Sweden (Kolitsch and Holtsman, 2004a) and within the Tisovec–Rejkovo rhyolite, Slovakia (Ondrejka et al., 2007). However, all the studies conducted so far on the samples from Mt. Cervandone, Italy, show the presence of a miscibility gap between the arsenate and phosphate end-members (Graeser and Schwander, 1987; Demartin et al., 1991). Monazite and xenotime are two of the most widespread REE-bearing minerals and are, along with the carbonate bastnäsite ($Ce(CO_3)F$), the major ores exploited for REE. Monazite-(Ce) represents the most common

form of monazite, whereas the natural La-, Nd- and Sm-dominant forms are fairly rare (Fleischer and Altschuler, 1969; Rosenblum and Fleischer, 1995; Long *et al.*, 2012). Monazite-(Ce) is a rather common accessory mineral in different geological settings, including granites, aluminous metamorphic rocks (e.g. amphibolites or medium- to high-grade pelitic rocks), carbonatites, pegmatites and hydrothermal veins (Cesbron, 1989). Moreover, monazite-(Ce) is also a common detrital mineral in sedimentary placers and a newly formed phase during diagenesis (Sengupta and Van Gosen, 2016; Čopjaková *et al.*, 2011). Xenotime-(Y) is an accessory component in several metasedimentary or igneous rocks, hydrothermal systems and early diagenesis environments (Spear and Pyle, 2002; Richter *et al.*, 2018).

In this work, focused on the case study of the Alpine quartz fissures (related to pegmatites overprinted by amphibolite facies) of Mt. Cervandone, the crystal chemistry and structure of chernovite-(Y), gasparite-(Ce), xenotime-(Y) and monazite-(Ce) is reinvestigated using electron probe microanalysis in wavelength dispersion spectroscopy mode (EPMA-WDS) and single-crystal X-ray diffraction. In addition, a comparative analysis of the crystal chemistry of chernovite-(Y), on the basis of literature data (Breiter *et al.*, 2009; Förster *et al.*, 2011; Kerbey, 2013, Papoutsa and Pe-Piper, 2014; Li *et al.*, 2019) is given. This study is part of a broader project aimed at improving the knowledge on the hydrothermal mineral deposit of Mt. Cervandone and the role of REE on the minerals phase stability and structure-related properties (Gatta *et al.*, 2019; 2021).

Crystal structure of chernovite-(Y), gasparite-(Ce), xenotime-(Y) and monazite-(Ce)

The aforementioned ATO_4 minerals crystalise in a monoclinic monazite-type or in a tetragonal xenotime-type structure. The two structural models share a similar topology, characterised by the presence of chains, running along the [001] direction, made by the alternation of (REE)-polyhedra and tetrahedral units, the latter occupied mainly by As and P (Fig. 1c and d, respectively). In the monazite-type structure, space group $P2_1/n$, the REE cation is ninefold-coordinated in a distorted polyhedron (Clavier *et al.*, 2011). $REEO_9$-polyhedra and (As,P)-tetrahedra are edge-sharing connected to form infinite chains running along the *c* axis (Fig. 1c). The tetragonal zircon-type structure, space group $I4_1/amd$, shows the alternation of 8-coordinated (REE) polyhedra and tetrahedra, giving rise to infinite chains along [001] (Fig. 1d). Within the REE-bearing phosphates, the larger and lighter REE ranging from La to Eu are hosted preferentially by the monazite-type structure, whereas the smaller and heavier REE, from Tb to Lu, and including Y and Sc, fit best into the zircon-type structure (Mooney, 1948; Boatner, 2002; Ni *et al.*, 1995; Kolitsch and Holtstam, 2004b; Clavier *et al.*, 2011). For synthetic Gd, Tb and Dy phosphates, the possible presence of two coexisting polymorphs is observed: they may crystallise in both monazite- and zircon-type structures. A similar behaviour has been reported for the $REEAsO_4$ series: the monoclinic structure preferentially hosts the larger REE (from La to Nd), whereas the smaller REE (from Sm to Lu, as well as Y and Sc) are hosted preferentially by the tetragonal crystal structure (Ushakov *et al.*, 2001; Boatner *et al.*, 2002).

Geological background

The Mt. Cervandone mineral deposit is renowned for the discoveries of several REE-bearing minerals. These minerals are hosted

within Alpine fissures in quartz veins (e.g. Graeser and Albertini, 1995), closely related to pegmatitic dykes (Guastoni *et al.*, 2006). These dykes, tens of cm thick, intrude fine-grained two-mica leucocratic gneisses, metamorphosed under amphibolite-facies conditions (Dal Piaz, 1975), and extend for hundreds of metres within the 'Mount Leone–Arbola' nappe, being concordant with the gneiss schistosity. The dykes show a pegmatitic texture and a strong NYF (niobium–yttrium–fluorine) chemical signature (Černý, 1991a,b; Ercit *et al.*, 2005; Černý and Ercit, 2005), which is reflected in the formation of Be–As–Nb–REE minerals, represented here by allanite-(Ce) and REE-bearing carbonates, arsenates, phosphates and oxides. Locally, the pegmatitic dykes are interrupted by discordant, subvertical quartz veins, composed mainly by vitreous and smoky quartz and muscovite. These quartz veins commonly contain open Alpine-type fissures, which host several REE-bearing accessory minerals, including cafarsite, synchysite-(Ce), chernovite-(Y), gasparite-(Ce), xenotime-(Y) and monazite-(Ce). Rutile, magnetite, hematite, titanite and tourmaline represent other common accessory minerals within these fissures. During the Alpine orogenic event, the circulation of hydrothermal fluids within the pegmatitic dykes, strongly enriched in arsenic, led to the mobilisation of Y, Nb, Ta, REE, Th and U. Subsequently, the circulating hydrothermal fluids led to the formation of the aforementioned quartz veins with the concomitant precipitation of As-, P- and REE-enriched minerals (Guastoni *et al.*, 2006; Gatta *et al.*, 2018).

Unfortunately, no data on the temperatures of the hydrothermal fluids of this area are available. The discussion of the experimental data (below), is somewhat hindered by the complexity of the geological evolution of the area, characterised by several different phases and fluids of different nature within the vein system.

Materials and methods

Fourteen rock specimens, from different Alpine quartz fissures, cropping out at Mt. Cervandone, containing REE-bearing arsenates and phosphates, have been selected for this investigation. They were first observed under a stereomicroscope to identify their mineralogical assemblage, which was later confirmed by single-crystal X-ray diffraction. Table 1 reports the mineral association within each rock sample, coupled with a specific label for the REE-bearing minerals. Fifteen REE-bearing phosphate and arsenate crystals have been selected and extracted from the fourteen rock specimens under study (see Table 1), and then characterised by means of electron probe microanalysis in wavelength dispersion spectroscopy mode (EPMA-WDS) and single-crystal X-ray diffraction.

Sample description

Chernovite-(Y) occurs as idiomorphic bipyramidal or prismatic crystals, as well as micrometric aggregates (Fig. 2). Bipyramidal crystals represent the most common form: they were identified within the samples Ch6, Ch7, Ch8, Ch9, Ch10 (Fig. 2a), Ch12 (Fig. 2c) and Ch13. Xenotime-(Y) also has a bipyramidal habit (Fig. 2f). Chernovite-(Y) forms idiomorphic crystals such as Ch11 (Fig. 2b) and Ch12 (Fig. 2c) or Ch13 and Ch16, ranging from 40 μm to 2 mm in size (Fig. 2d,e). Among the chernovites-(Y) crystals, only the Ch11 sample (Fig. 2b) shows a prismatic habit. The three monazite-(Ce) samples are euhedral and vitreous orangish aggregates (or millimetric crystals) (Fig. 3a), coupled with anhedral aggregates in Mon2 and Mon14. The samples of gasparite-(Ce) are characterised by brownish to green crystals (3 to 20 μm in diameter, Fig. 3b) clustered in aggregates. Both

Table 1. Mineralogical assemblage of each sample from the quartz Alpine-fissures of Mt. Cervandone (quartz is ubiquitous and not reported), identified by single-crystal X-ray diffraction, except for the ThSiO$_4$ grains.

Rock sample	REE-minerals	REE-mineral sample name	Associated accessory minerals
M-C1	Monazite-(Ce)	Mon1	Muscovite, magnetite, rutile, hematite
M-C2	Monazite-(Ce)	Mon2	Muscovite, magnetite, rutile, hematite, clinochlore
M-C3	Gasparite-(Ce)	Gasp3	Muscovite, magnetite, clinochlore
M-C4	Gasparite-(Ce)	Gasp4	Muscovite, magnetite, clinochlore
M-C6	Chernovite-(Y)	Ch6	Muscovite, magnetite
M-C7	Chernovite-(Y)	Ch7	Titanite, muscovite, magnetite
M-C8	Chernovite-(Y)	Ch8	Muscovite, magnetite, rutile, tourmaline
M-C9	Chernovite-(Y)	Ch9	Muscovite
M-C10	Chernovite-(Y)	Ch10	Muscovite, magnetite
M-C11	Chernovite-(Y)–xenotime(Y) s.s.	Ch11	Muscovite, magnetite, rutile, hematite, ThSiO$_4$ (thorite or huttonite)
M-C12	Chernovite-(Y)	Ch12	Muscovite
M-C13	Chernovite-(Y)	Ch13	Muscovite, clinochlore
M-C14	Xenotime-(Y), monazite-(Ce)	Xen14, Mon14	Muscovite, magnetite, rutile, hematite, ThSiO$_4$ (thorite or huttonite)
M-C16	Chernovite-(Y)	Ch16	Magnetite, plagioclase

samples of gasparite-(Ce) under investigation were formed by replacement of barrel-shaped crystals of synchysite-(Ce).

Electron microprobe analysis

The chemical composition of the REE-bearing phosphates and arsenates investigated was determined using a JEOL JXA–8200 electron microprobe at the Earth Sciences Dept. of the University of Milano (ESD-MI), operating in WDS mode with a focused beam (∼5 μm in diameter), an acceleration voltage of 20 kV and a beam current of 20 nA. The counting time was set to 30 s for peaks and 10 s for the background. Correction for matrix effects was applied using the *PhiRhoZ* method, as implemented in the JEOL suite of programs. The following natural and synthetic standards (with spectral lines) were used: grossular (Ca$K\alpha$ and Si$K\alpha$), nickeline (As$K\alpha$), synthetic YPO$_4$ (Y$L\alpha$ and P$K\alpha$), synthetic Ln(PO$_4$) set (La$L\alpha$, Ce$L\alpha$, Pr$L\alpha$, Nd$L\alpha$, Sm$L\alpha$, Eu$L\alpha$, Gd$L\alpha$, Tb$L\alpha$, Dy$L\alpha$, Ho$L\alpha$, Er$L\alpha$, Tm$L\alpha$, Yb$L\alpha$ and Lu$L\alpha$), synthetic UO$_2$ (U$M\beta$), synthetic ThO$_2$ (Th$M\alpha$) and galena (Pb$M\alpha$). Back-scattered (BSE) images were acquired (Fig. 4), together with EDS compositional maps for the Ch11 sample, detailing the concentrations of As, Ce, Sm and Th (Fig. 5). The average chemical composition for all the samples (excluding the more heterogeneous Ch13 and Ch16 specimens) is reported in Table 2. The chemical composition, expressed as oxide wt.% and atoms per formula unit (apfu), pertaining to all the analytical points, is reported in Supplementary material (Tables S1–S15).

### Single-crystal X-ray diffraction and structure refinement protocol

The single-crystal X-ray diffraction experiments were performed at the ESD-MI using a Rigaku XtaLAB Synergy-S diffractometer, equipped with a HyPix–6000HE HPC area detector and a PhotonJet-S Mo-$K\alpha$ (λ=0.71073 Å) microsource, operating at 50 kV and 1 mA. Each data collection was performed using a sample-to-detector distance of 62 mm and a step-scan width of 0.5°. The crystal size of all the samples investigated and the exposure times are reported in Supplementary Table S16. For all the collected datasets, indexing of the diffraction peaks, unit-cell refinement and intensity data reduction were performed using the *CrysAlisPro* software (Rigaku Oxford Diffraction, 2019). The unit-cell parameters for all the samples under investigation are reported in Table 3.

The structure refinements were performed using the *Jana2006* software (Petříček *et al.*, 2014), starting from the models reported by Strada and Schwendimann (1934) for chernovite-(Y), Ni *et al.* (1995) for xenotime-(Y), Kolitsch and Holtsman (2004a) for gasparite-(Ce) and Ni *et al.* (1995) for monazite-(Ce). The site occupancy factors of the A (REE-bearing) and tetrahedral sites were fixed according to the average chemical composition obtained from WDS analysis for each crystal sample (Table 2), leaving out the elements with a low concentration and assuming a full occupancy for both the sites. For the Ch11 and Ch13 samples, characterised by a significant chemical variability (Figs 4, 5; Supplementary Tables S10, S12), the same strategy has been followed, however the relative occupancies of the different chemical species have been varied (keeping the consistency with the measured chemical data) in order to obtain the best figures of merit of the structure refinements. Each structure refinement was performed adopting anisotropic displacement parameters. All the refinements converged with no significant correlations among the refined variables. The refined structure models are deposited as crystallographic information files and are available as Supplementary material (see below). Some relevant structural features, including the interatomic bond distances and the volumes of the coordination polyhedra, are reported in Table 4.

Results and discussion

Chemical composition and REE pattern

The average chemical composition of the samples Mon1, Mon2, Gasp3, Gasp4, Ch6, Ch7, Ch8, Ch9, Ch10, Ch11, Ch12, Xen14 and Mon14 are given in Table 2, while Supplementary Tables S12 and S15 report the results from each point analysis of the chemically heterogeneous samples, Ch13 and Ch16. For Ch11, the average chemical compositions of four domains, identified from EPMA compositional maps (Fig. 5), are labelled as Ch11$_a$ Ch11$_b$, Ch11$_c$ and Ch11$_d$. Thorium shows the most variable content, for both zircon- and monazite-type minerals. The enrichment of Th within the REETO_4 compounds is controlled by two potential substitution mechanisms:

$$(Th, U)^{4+} + Ca^{2+} = 2REE^{3+} \tag{1}$$

$$(Th, U)^{4+} + Si^{4+} = REE^{3+} + (P, As)^{5+} \tag{2}$$
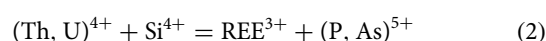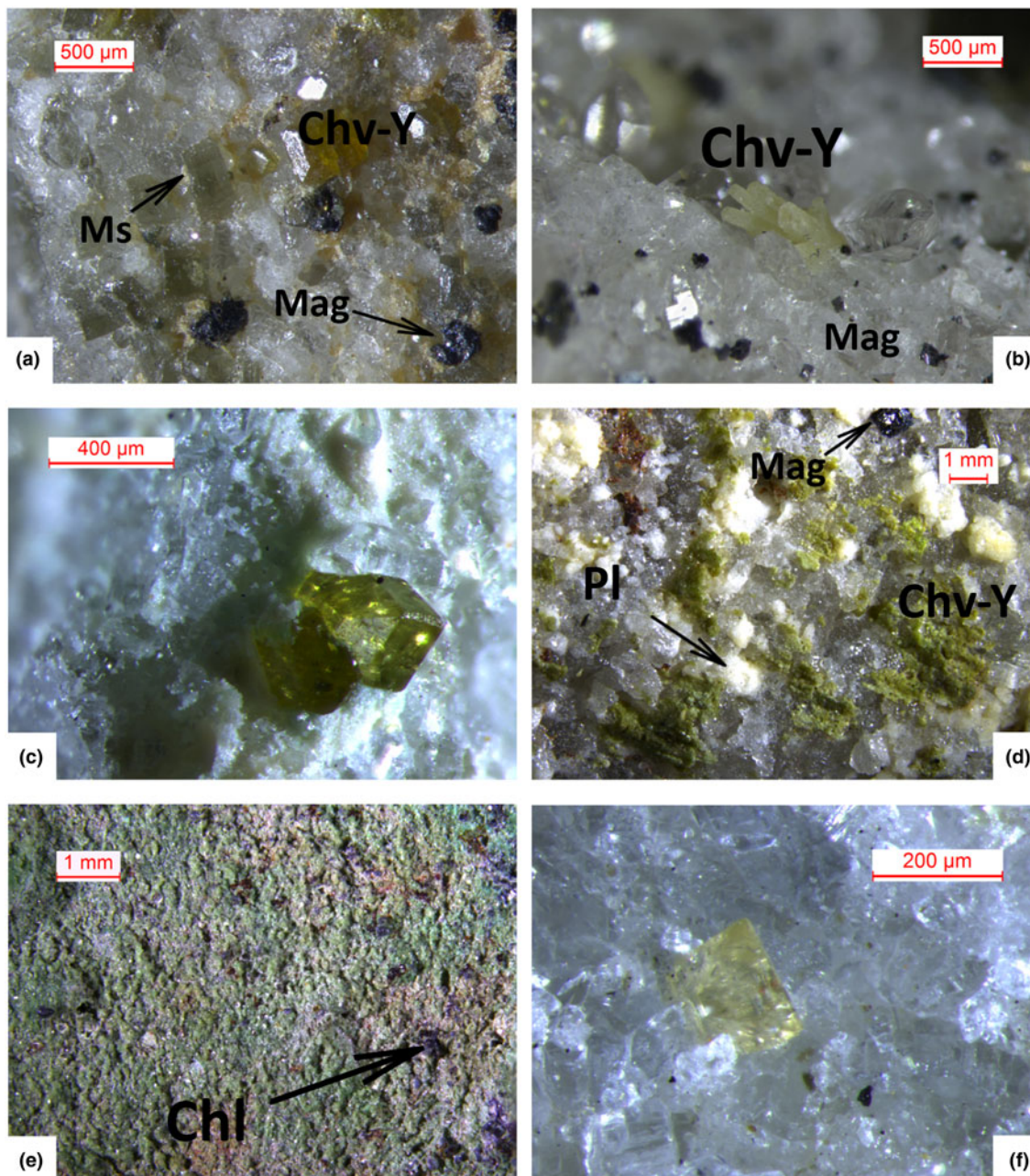
Fig. 2. Photographs of selected samples from the Alpine quartz fissures of Mt. Cervandone bearing REE-phosphates and -arsenates: (a) yellow Ch10 chernovite-(Y) sample with magnetite and muscovite on quartz; (b) prismatic Ch11 chernovite-(Y) sample with magnetite grains on quartz; (c) yellow Ch12 chernovite-(Y) sample on quartz; (d) greenish microcrystals of Ch16 chernovite-(Y) sample, with plagioclase and magnetite, on quartz; (e) M-C13 orthogneiss lined with several Ch13 chernovite-(Y) microcrystals and few grains of clinochlore; (f) bipyramidal crystal of Xen14 xenotime-(Y) on quartz (see also Table 1). [Chv-Y: chernovite-(Y); Mag: magnetite; Ms: muscovite; Pl: plagioclase; Chl: clinochlore. Warr (2021)].

known as cheralite (equation 1) and thorite substitution mechanisms (equation 2). Plotting the data in a P/(P+As+Si) *vs.* Y diagram (Fig. 6a), clearly distinguishes the four minerals under investigation into four distinct domains. The Y-poor side of the diagram contains the chemical data from the monazite-(Ce) and gasparite-(Ce) crystals, enriched in P and As, respectively. Data from chernovite-(Y) and xenotime-(Y) lie on the Y-enriched side of the diagram, and are characterised by a highly variable P and As fraction, resulting in an almost complete solid solution along the join chernovite-(Y)–xenotime-(Y) (as also shown by the chemical compositions of samples Ch11 and Ch16, having equal fractions of As and P). On the contrary, the composition of gasparite-(Ce) and monazite-(Ce) crystals is closer to the ideal end-members, and only a partial solution is observed. Monazite-(Ce) and gasparite-(Ce) are characterised by a poor Y content, coupled with an enrichment in LREE elements, with Ce (on average, 0.46(2) apfu) as the most common cation, followed by La (0.20(2) apfu) and Nd (0.17(2) apfu).

The *A*-site of the chernovite-(Y)–xenotime-(Y) series is characterised by a relatively constant composition, where Y is always the dominant cation (ranging from a maximum of 0.78 apfu to a minimum of 0.46 apfu), followed, on average, by Dy, Er, Gd,

Fig. 3. Photographs of two samples of the gasparite-(Ce)–monazite-(Ce) series: (a) Mon2 monazite-(Ce) sample, with rutile (red); (b) greenish, barrel-shape Gasp4 gasparite-(Ce) sample, pseudomorph after synchysite-(Ce), with clinochlore grains, on quartz. [Rt: rutile; Mnz-Ce: monazite-(Ce); Gsp-Ce: gasparite-(Ce); Chl: clino-chlore. Warr, 2021].
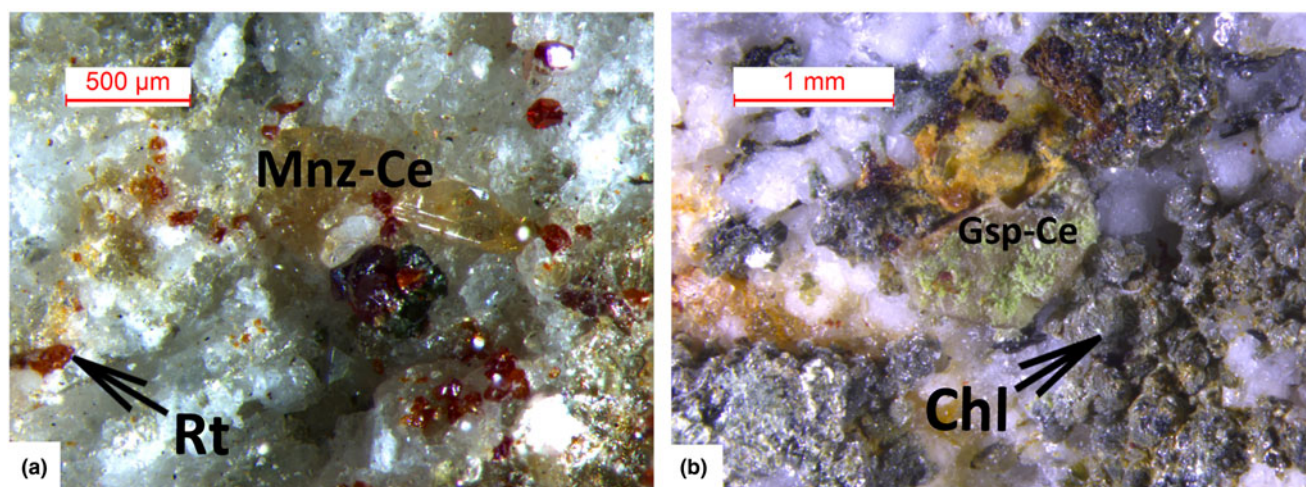
Yb and Ho. When the Y content is lower than ~0.6 apfu, Th or LREE become relevant A-site occupying cations. The fraction of LREE in chernovite-(Y) and xenotime-(Y) is generally low (see below for further details), reaching its maximal values in a few analytical data points for Ch11. The REE pattern for all the samples under investigation is reported in Fig. 7, normalised to the REE concentration of the Carbonaceous Chondrite CN-1, after Wasson and Kallemeyn (1988). For all the points, the abundance of Eu is lower than the detection limit. As mentioned above, the tetragonal structure of chernovite-(Y) and xenotime-(Y) has a strong preference for Y and, in general, the smaller HREE: this pattern is reflected by the positive slope reported in Fig. 7b. Conversely, in the gasparite-(Ce)–monazite-(Ce) series, the LREE enrichment is responsible for the negative slope in Fig. 7a. It is worthwhile pointing out that the relatively high Gd content, shown by the three monazites under investigation, has been described already in alpine-fissure minerals related to the circulation of hydrothermal fluids, as in the case of Mt. Cervandone (Demartin et al., 1991; Della Ventura et al., 1996). Due to their low content (<0.002 apfu), Er–Lu elements are not reported in Fig. 7a. In addition, the Carbonaceous Chondrite CN-1 REE-normalised diagram reported in Fig. 7b shows that there is a positive anomaly in the Ho and Lu concentrations in chernovite-(Y) and xenotime-(Y) from Mt. Cervandone. Literature data (Ondrejka et al., 2007; Förster et al., 2011; Papoutsa and Pe-Piper, 2014), reporting the Ho and Lu contents in chernovite-(Y) and xenotime-(Y) samples, reveal that the maximum Ho_2O_3 content detected in chernovite-(Y) is 2.44 wt.% (Papoutsa and Pe-Piper, 2014), slightly lower than the highest average content of the samples of this study (Table 2), whereas Förster et al. (2011) reported the maximum content of Lu_2O_3 as 1.29 wt.%, very close to that of the samples of this study (Table 2). Although a correction protocol for REE interferences has been applied to the experimental chemical data of this study, we cannot unambiguously exclude that the observed anomalies may be slightly affected by the adopted experimental strategy. However, the previous findings reported in the literature (e.g. Ondrejka et al., 2007; Förster et al., 2011; Papoutsa and Pe-Piper, 2014) corroborate the results of this study.

Chemical composition of the chernovite-(Y)–xenotime-(Y) series
Although the trivalent cations are always dominant within the A-site of the tetragonal series, some data points from samples Ch6, Ch10, Ch11, Ch13 and Ch16 show a relatively large amount of Th. The thorite substitution mechanism (equation 2) probably occurs in the chernovite-(Y)–xenotime-(Y) series under investigation, as suggested by the strong positive linear correlation between Si and the Th+U fraction (Fig. 6b). For a better representation of the crystal-chemistry of the mineral samples of this study, the (tetragonal) 2-component system chernovite-(Y)–xenotime-(Y) could be replaced by a 3-component solid solution between the end-members chernovite-(Y), xenotime-(Y) and $ThSiO_4$ (Fig. 8). From Fig. 8, as well as in the P/(P+As+Si) vs. Y diagram (Fig. 6a), even in the more P-depleted samples (i.e. Ch6, Ch7, Ch8, Ch9, Ch10 and Ch12), the concentration of this element is relatively high, with an average of 20(3) mol.% of xenotime-(Y) component, coupled with a very small $ThSiO_4$ fraction (on average 3(1) mol.%). Conversely, the xenotime-(Y) sample Xen14 shows a chemical composition (Table 2) much closer to the ideal end-member, with As usually low, corresponding to an average chernovite-(Y) component between 7.0 mol.% and 12.9 mol.%. Between the chernovite-(Y)–xenotime-(Y) edge and the $ThSiO_4$ corner, the samples investigated show that a wide miscibility gap occurs (Fig. 8).

The most Th-enriched analyses on the chernovite-(Y)–xenotime-(Y) edge belong to Ch13 and Ch16 (Fig. 8), which are also characterised by a highly altered texture (Fig. 4f) and variable composition. In these cases, the major chemical variations concern a strong Th-enrichment, reflected by a $ThSiO_4$ component ranging from 4.7 mol.% to 15.3 mol.% for Ch13, and between 1.3 mol.% and 12.3.% for Ch16. The relatively large fraction of the $ThSiO_4$ component may be responsible for the greenish colour observed only in these samples (Fig. 2d,e). Moreover, these samples are also characterised by a larger fraction of CaO (up to 1.93 wt.%, in Ch16, compared to an average 0.1(3) wt.% for the other chernovite-(Y) samples), suggesting the occurrence of the cheralite substitution mechanism (equation 1). In addition, Ch16 reveals the presence of P-enriched domains, with a maximum xenotime-(Y) component of 45.10 mol.% (Fig. 8). The P- and the As-enriched domains are linked by an irregular lobate interface, as shown in Fig. 4f.
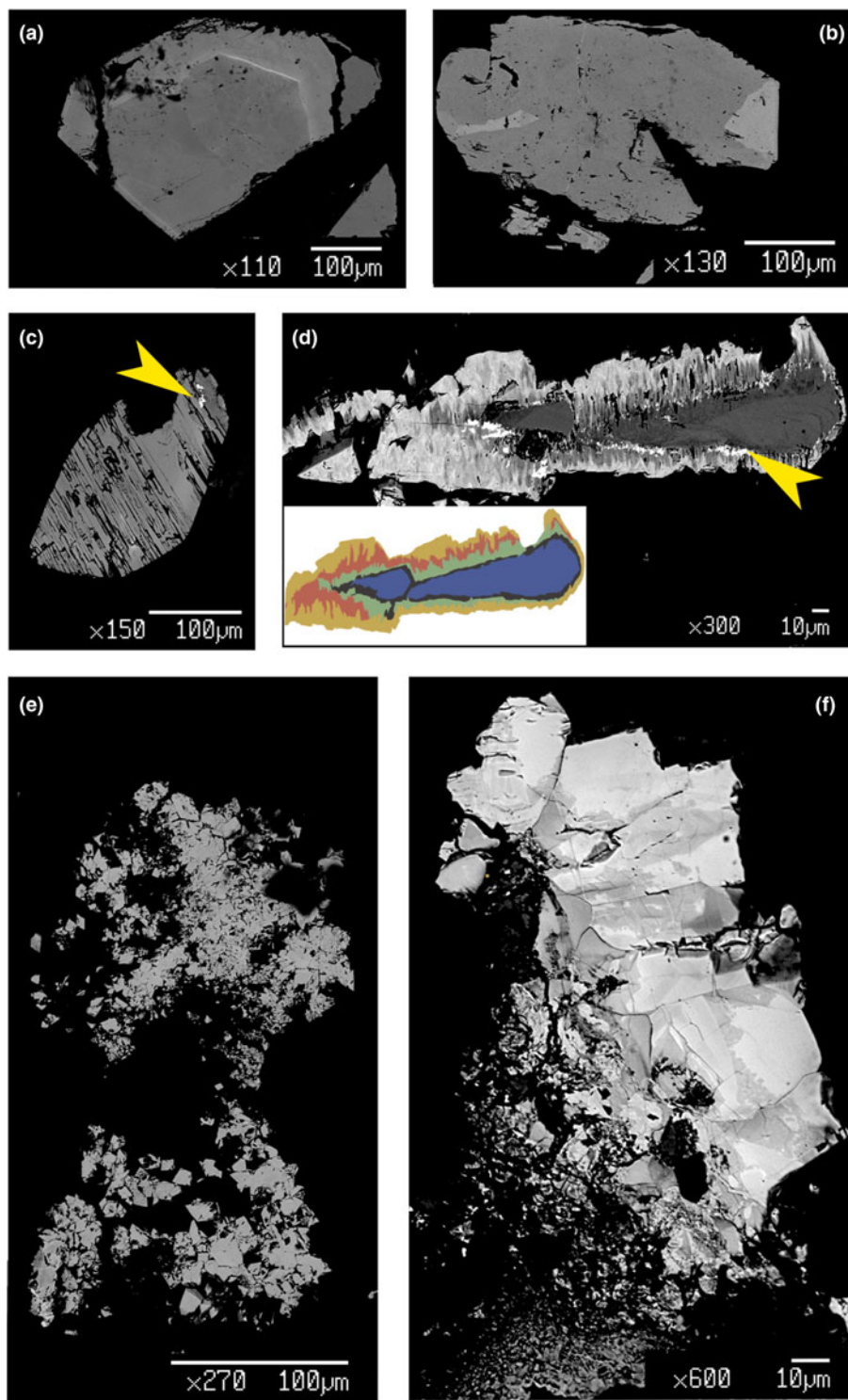
Fig. 4. BSE images of selected samples under investigation: (a) *quasi*-homogeneous crystal of Ch10, containing a brighter $ThSiO_4$-enriched level; (b) crystal of Mon2 monazite-(Ce) sample, showing brighter domains characterized by a higher Th content; (c) chemically-homogeneous and fractured Xen14 xenotime-(Y) sample, containing $ThSiO_4$ grains (indicated by the yellow arrow); (d) highly zoned Ch11 sample, showing five main domains highlighted with different colours in the insert (see Fig. 5 and text), with $ThSiO_4$ grains indicated by the yellow arrow; (e) gasparite-(Ce) sample, Gasp3, comprising several microcrystals (~10 μm size); (f) highly-zoned Ch16 chernovite-(Y) sample, containing P-enriched darker patchy domains and brighter As-enriched domains, separated by lobate interface.

As mentioned above, the Ch11 sample (Fig. 4d and Fig. 5) shows a clear core-to-rim zonation, which is characterised by a P-enriched core and an As- and LREE-enriched rim (Fig. 7). EPMA X-ray compositional maps for the Ch11 sample (Fig. 5), showing the fraction of As (Fig. 5a), Ce (Fig. 5b), Sm (Fig. 5c) and Th (Fig. 5d), allow a subdivision into five domains: (1) a *quasi*-homogeneous core (Ch11$_a$; the blue-coloured area of the insert of Fig. 4d), characterised by an intermediate composition between chernovite-(Y) and xenotime-(Y), with a slight predominance of the latter (up to 60.86 mol.% of xenotime-(Y) component) as reported in Table 2; (2) a segment enriched in $ThSiO_4$ (thorite or huttonite) inclusions in the form of grains (~1–5 μm in size), clearly visible in Fig. 4d (black area within the insert) and Fig. 5d; (3) an interface zone (Ch11$_b$; green area in the insert of Fig. 4d), characterised by an almost equal amount of P and As (xenotime-(Y) molar abundance reaches 52.68 mol.%, slightly lower than the inner, darker core), as well as an enrichment in Th; (4) a chernovite-(Y) domain (Ch11$_c$; red area in
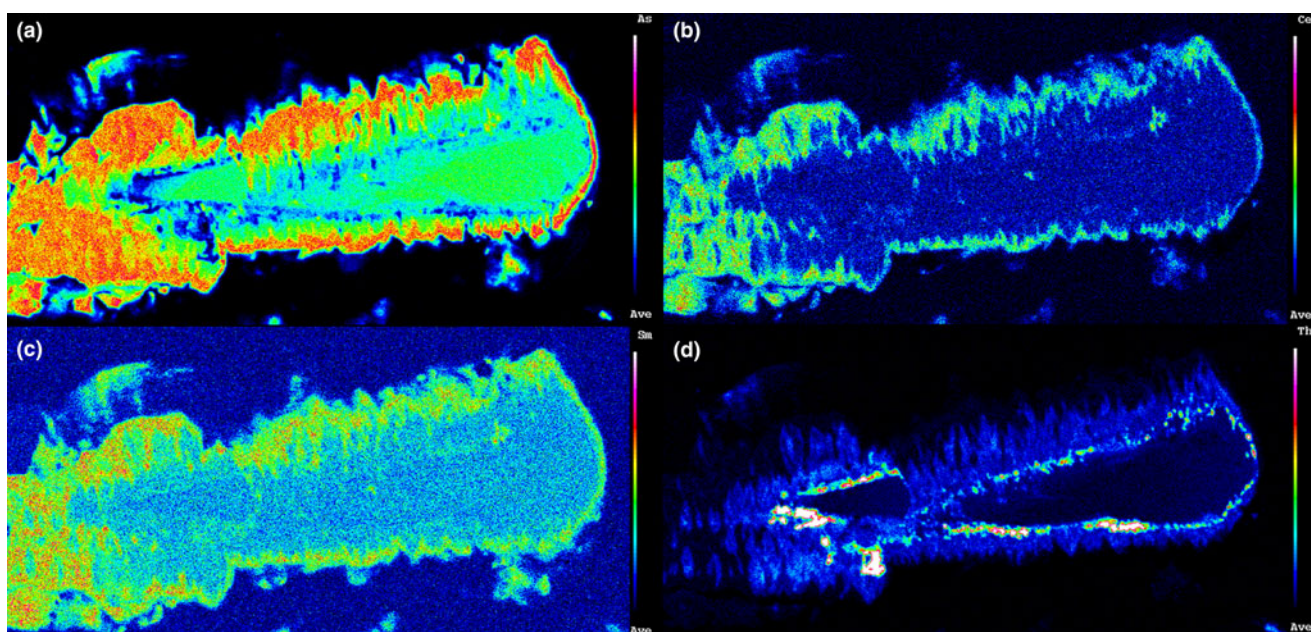
Fig. 5. Compositional maps for the Ch11 chernovite-(Y) sample, showing the distribution of (a) As, (b) Ce, (c) Sm and (d) Th.

the insert of Fig. 4d), with high HREE and Th; (5) a relatively Th-poor outer domain (Ch11$_d$; the yellow area in the insert of Fig. 4d), characterised by an enrichment in LREE, as shown by the increase in the Ce and Sm fraction towards the rim (Fig. 5b and Fig. 5c), coupled with the highest As content (Fig. 5a). The contact between Ch11$_b$ and Ch11$_c$, as well as between Ch11$_c$ and Ch11$_d$, is marked by a discontinuous flame-like interface. The most As-enriched points of the EPMA–WDS data (up to 98.82 mol.% of the (REE)AsO$_4$ component) refers to the Ch11$_d$ domain and also show the highest LREE and lowest Th concentration within the chernovite-(Y)–xenotime-(Y)–ThSiO$_4$ solid solution: Y is still the most abundant *A* cation (0.487 apfu), but is depleted with respect to the inner portions and the other chernovite-(Y) samples (ca. 0.6–0.8 apfu; Table 2). Nd is the second most abundant *A* cation, and significant fractions of Sm, Ce and Pr are also present, up to 10.80 wt.% for Nd$_2$O$_3$ (0.167 apfu *vs.* <0.01 apfu in the other chernovites), 5.18 wt.% for Sm$_2$O$_3$ (0.077 apfu *vs.* <0.015 apfu), 3.87 wt.% for Ce$_2$O$_3$ (0.061 apfu *vs.* <0.003 apfu) and 1.23 wt.% for Pr$_2$O$_3$ (0.019 apfu *vs.* substantially absent in other chernovites). Overall, a comparative analysis of the *A*-site composition of the chernovite-(Y) and xenotime-(Y) crystals does not reveal a preferential partitioning of Y and the other HREE among the investigated zircon-type tetragonal arsenates and phosphates (Fig. 7a and Supplementary Tables S1–15). However, the chemical heterogeneity and altered texture of some samples (e.g. Ch11, Ch13 and Ch16) suggests a complex interplay with chemically variable hydrothermal fluids, which may have led to local chemical dissolutions of P-enriched chernovites-(Y) and precipitation of ThSiO$_4$ crystals. The identification of these crystals as thorite (isostructural with zircon) or huttonite (isostructural with monazite) is not straightforward. The phase stability relationships between the two ThSiO$_4$ polymorphs have been discussed widely by several authors (Harlov *et al.*, 2007; Mazeina *et al.*, 2005; Seydoux and Montel, 1997), reporting that huttonite is stable at higher *T* and *P* with respect to thorite. However, the presence of REE at the *A*-site, according to Speer and Cooper (1982), may enlarge the stability field of

huttonite to lower temperatures. Harlov *et al.* (2007) found that the crystallisation of metastable huttonite at the expense of monazite-(Ce) crystals can take place at 400°C (and 500 MPa), in the thorite field, as also reported by Guastoni *et al.* (2016) for pegmatitic monazites of the Central Alps. In this light, given the difficulty of differentiating between thorite and huttonite by means of EPMA (Harlov *et al.*, 2002; Harlov and Föster, 2002) and the lack of information on the (*P,T*) conditions of the hydrothermal fluids of Mt. Cervandone, it is impossible to identify unambiguously which polymorph of ThSiO$_4$ is associated with the zircon-type and monazite-type REE*T*O$_4$ minerals of this study.

The sample Ch11 shows the presence of a reaction contact. In this case, a Th-rich layer, i.e. Ch11$_b$ (see Figs 4, 5), represents the reactional crown around the more chemically homogeneous Ch11$_a$. The few ThSiO$_4$ grain inclusions present show a chemical composition related closely to the surroundings: ThSiO$_4$ shows an As-enrichment over P, when in contact with the chernovite-(Y)–xenotime-(Y) s.s. (Ch11) and an evident P-enrichment when included in the Xen14 grains (Supplementary Table S13). The three points of analysis falling into the ThSiO$_4$ field (Fig. 8) are characterised by a REE-pattern (Supplementary Fig. S1) in which, considering only the lanthanides, the HREE slightly prevail over the LREE. This pattern probably reflects the chemical composition of the hydrothermal fluids, which may be affected and, in turn, modified in response to several processes. These may include, but are not limited to, the destabilisation of REE-enriched minerals as, for example, allanite and gadolinite, as well as a different partitioning of the different REE's as trace elements in nominally REE-free minerals. The paramount role of water in stabilising the actinides and Ln orthosilicates has been suggested by several authors (e.g. Johan and Johan, 2005; Strzelecki *et al.*, 2021) and the hydroxilised nature of the ThSiO$_4$ grain inclusions could explain the poor closure of their EPMA data. Moreover, Mesbah *et al.* (2016) identified a complete solid solution between the zircon-type ErPO$_4$ and thorite, synthesised under hydrothermal conditions (250°C). However, in the natural samples investigated here a very sharp contact (Fig. 4c,d) has been observed between the ThSiO$_4$ grains and the surrounding phosphates and arsenates.

Table 2. Average chemical composition (expressed in oxide wt.% and in atoms per formula unit (apfu) calculated on the basis of 4 oxygen atoms) of all the samples under investigation (except for the heterogeneous Ch13 and Ch16 specimens, the compositions of which are reported in Table S12 and Table S15, respectively). For the sample Ch11, the average composition of four distinct domains is reported as Ch11$_a$ (P-enriched core), Ch11$_b$ (P- and Th-enriched intermediate zone), Ch11$_c$ (P-depleted and Th-enriched intermediate zone) and Ch11$_d$ (P-depleted and LREE-enriched outer rim) [see text and Figs 4, 5 for further details].

	Mon1		Mon2		Gasp3		Gasp4		Ch6		Ch7	
As_2O_5	0.15	(0.09–0.23)	2.26	(1.40–3.14)	38.61	(36.38–40.59)	41.39	(38.45–42.97)	33.41	(30.14–35.61)	37.10	(32.82–39.44)
P_2O_5	28.64	(28.33–29.00)	27.77	(26.69–28.62)	0.83	(0.25–3.01)	0.13	(0–0.61)	7.81	(2.17–10.1)	5.29	(4.01–8.87)
SiO_2	0.21	(0.05–0.37)	0.24	(0.09–0.59)	1.72	(1.21–2.39)	1.48	(0.58–3.11)	0.65	(0.39–3.17)	0.76	(0.29–1.08)
V_2O_5	b.d.l.		b.d.l.		b.d.l.		b.d.l.		0.01	(0–0.07)	0.02	(0–0.10)
CaO	1.40	(0.88–1.65)	0.68	(0.20–1.22)	1.46	(1.22–1.79)	1.92	(1.64–2.26)	0.02	(0–0.06)	0.01	(0–0.03)
Y_2O_3	0.90	(0.65–1.12)	0.52	(0.43–0.67)	0.01	(0–0.07)	0.05	(0–0.19)	33.97	(25.38–35.05)	35.87	(35.11–37.17)
La_2O_3	13.24	(12.12–14.76)	13.08	(12.39–14.53)	11.38	(10.74–12.16)	12.86	(10.89–14.43)	0.04	(0–0.22)	0.05	(0–0.16)
Ce_2O_3	29.88	(28.77–31.23)	31.31	(29.13–32.61)	28.3	(27.08–31.19)	26.86	(24.56–27.95)	0.13	(0.01–0.37)	0.12	(0–0.20)
Pr_2O_3	3.28	(2.79–3.45)	3.70	(3.10–4.03)	2.98	(2.68–3.38)	2.56	(1.92–2.82)	0.04	(0–0.17)	b.d.l.	
Nd_2O_3	12.93	(12.15–14.36)	13.70	(12.72–15.03)	11.63	(10.26–12.75)	9.40	(8.03–10.2)	0.58	(0.38–2.20)	0.25	(0.07–0.35)
Sm_2O_3	2.51	(2.07–3.21)	2.51	(2.28–2.81)	1.43	(0.90–1.84)	1.22	(0.91–1.48)	0.96	(0.73–2.36)	0.43	(0.22–0.61)
Eu_2O_3	b.d.l.		b.d.l.		b.d.l.		b.d.l.		b.d.l.		b.d.l.	
Gd_2O_3	1.88	(1.33–2.33)	1.48	(1.17–1.93)	0.38	(0.04–0.62)	0.62	(0.31–0.97)	2.58	(2.10–4.52)	1.58	(1.38–1.85)
Tb_2O_3	b.d.l.		b.d.l.		b.d.l.		b.d.l.		0.59	(0.31–0.77)	0.46	(0.29–0.62)
Dy_2O_3	0.39	(0.18–0.70)	0.30	(0.11–0.49)	0.03	(0–0.13)	0.04	(0–0.22)	4.86	(4.45–5.36)	4.07	(3.68–4.41)
Ho_2O_3	0.45	(0.21–0.75)	0.32	(0.01–0.54)	b.d.l.		0.03	(0–0.16)	2.39	(2.11–3.05)	1.87	(1.57–2.28)
Er_2O_3	0.02	(0–0.10)	b.d.l.		0.03	(0–0.13)	0.03	(0–0.23)	3.38	(2.23–3.85)	3.36	(3.20–3.72)
Tm_2O_3	0.08	(0–0.30)	0.04	(0–0.32)	0.03	(0–0.15)	0.01	(0–0.13)	0.42	(0.11–0.62)	0.36	(0.18–0.53)
Yb_2O_3	0.01	(0–0.08)	0.01	(0–0.06)	0.04	(0–0.16)	0.04	(0–0.22)	2.91	(1.73–3.20)	2.94	(2.56–3.25)
Lu_2O_3	0.15	(0.02–0.46)	0.10	(0–0.34)	0.04	(0–0.14)	0.05	(0–0.16)	1.21	(0.82–1.54)	0.99	(0.74–1.33)
PbO	0.02	(0–0.12)	0.01	(0–0.05)	0.02	(0–0.09)	0.05	(0–0.21)	0.19	(0–0.37)	0.29	(0.13–0.40)
ThO_2	3.10	(1.47–4.52)	2.32	(0.90–5.30)	0.90	(0.13–2.23)	1.96	(0–9.13)	2.51	(1.72–10.8)	0.78	(0.33–0.99)
UO_2	0.05	(0–0.20)	0.13	(0.00–0.23)	b.d.l.		0.06	(0–0.26)	0.91	(0.60–1.96)	3.39	(2.08–4.04)
Total	99.39		100.60		99.91		100.87		99.76		100.10	
Atoms per formula unit (apfu) calculated on the basis of 4 oxygen atoms												
As	0.003		0.047		0.913		0.964		0.698		0.777	
P	0.968		0.933		0.031		0.005		0.264		0.179	
Si	0.008		0.009		0.078		0.066		0.026		0.030	
V	–		–		–		–		–		–	
Ca	0.060		0.029		0.071		0.092		0.001		0	
Y	0.019		0.011		–		0.001		0.723		0.765	
La	0.195		0.191		0.189		0.211		–		–	
Ce	0.436		0.455		0.468		0.438		0.002		0.001	
Pr	0.047		0.053		0.049		0.041		0		–	
Nd	0.184		0.194		0.188		0.149		0.008		0.003	
Sm	0.034		0.034		0.022		0.019		0.013		0.005	
Eu	–		–		–		–		–		–	
Gd	0.024		0.019		0.005		0.009		0.042		0.042	
Tb	–		–		–		–		0.007		0.006	
Dy	0.005		0.003		–		0.001		0.062		0.052	
Ho	0.005		0.004		–		–		0.030		0.023	
Er	–		–		–		–		0.022		0.007	
Tm	0.001		–		–		–		0.005		0.004	
Yb	–		–		0.001		0.001		0.035		0.035	
Lu	0.002		0.001		0.001		0.001		0.014		0.012	
Pb	–		–		–		–		0.002		0.003	
Th	0.028		0.021		0.009		0.019		0.022		0.007	
U	0.001		0.001		–		–		0.008		0.030	

b.d.l.: below the detection limit

Chemical features of the gasparite-(Ce)–monazite-(Ce) series

All the gasparite-(Ce) and monazite-(Ce) samples show a rather similar composition of the ninefold-coordinated *A* site and the main differences in particular concern the abundance of Y and Ca. A relatively high amount of Y (Y_2O_3 on average, 0.7(2) wt.%) is shown by the three monazite-(Ce) samples, especially by the Mon1 sample (Y_2O_3 up to 1.12 wt.%), whereas this element is almost absent in the two gasparite-(Ce) samples (Y_2O_3 < 0.13 wt.%). Unlike monazite-(Ce), gasparite-(Ce) shows a higher content and more uniform distribution of Ca [CaO 1.8(2) wt.%, *vs* 1.1(4) wt.% for monazite-(Ce)]. Also in the gasparite-(Ce)–monazite-(Ce) series, Th has been found as the most variable element and, in addition, gasparite-(Ce) incorporates the highest fraction of Si among the investigated REE minerals (see Table 2). In this

case, a further charge-compensating mechanism should be involved, to fully explain the anomalous amount of Ca and Si, not compensated by Th+U, in gasparite-(Ce). The presence of monovalent anions, such as OH^-, F^- or Cl^-, in place of O^{2-}, may compensate for the presence of Si and Ca, according to the following equation:

$$2(OH, F, Cl)^- + Ca^{2+} + Si^{4+} = 2O^{2-} + REE^{3+} + (P, As)^{5+}$$

(3)

According to equation 3, if just OH^- is taken into account, the corresponding amount of H_2O necessary to compensate the charge defect is, on average, ~0.45 wt.% for both Gasp3 and

Table 2. (Continued)

	Ch8		Ch9		Ch10		Ch11_a		Ch11_b	
Wt.%										
As_2O_5	36.12	(34.22–37.14)	36.26	(34.38–38.83)	36.11	(34.77–36.91)	21.53	(19.55–22.21)	23.27	(21.75–23.39)
P_2O_5	5.41	(4.63–7.14)	5.64	(3.94–7.27)	5.41	(3.93–6.86)	18.73	(17.24–19.10)	15.81	(14.62–16.05)
SiO_2	0.67	(0.43–0.76)	0.62	(0.16–0.81)	0.82	(0.45–1.59)	0.11	(0.04–0.17)	0.87	(0.83–0.86)
V_2O_5	0.01	(0–0.04)	0.01	(0–0.03)	0.01	(0–0.05)	0.02	(0.00–0.04)	b.d.l.	
CaO	b.d.l.		0.01	(0–0.05)	0.01	(0–0.03)	0.02	(0–0.04)	0.01	(0.00–0.02)
Y_2O_3	34.30	(33.67–35.22)	34.31	(33.70–35.01)	33.10	(29.91–35.38)	39.24	(38.03–38.10)	36.94	(35.59–36.07)
La_2O_3	0.03	(0–0.10)	0.06	(0–0.14)	0.01	(0–0.05)	0.01	(0–0.02)	b.d.l.	
Ce_2O_3	0.09	(0–0.19)	0.14	(0–0.28)	0.13	(0.01–0.25)	0.03	(0–0.07)	0.10	(0.10–0.10)
Pr_2O_3	0.02	(0–0.12)	0.05	(0–0.14)	0.04	(0–0.09)	0.03	(0–0.06)	0.03	(0–0.06)
Nd_2O_3	0.37	(0.09–0.54)	0.37	(0.19–0.53)	0.37	(0.03–0.65)	0.36	(0.30–0.39)	0.40	(0.35–0.42)
Sm_2O_3	0.86	(0.65–0.97)	0.72	(0.34–0.93)	0.73	(0.55–1.06)	0.74	(0.68–0.75)	0.56	(0.41–0.68)
Eu_2O_3	b.d.l.		b.d.l.		b.d.l.		b.d.l.		b.d.l.	
Gd_2O_3	2.98	(2.64–3.35)	2.92	(1.82–3.45)	2.30	(1.73–3.07)	2.11	(1.99–2.11)	1.98	(1.89–1.94)
Tb_2O_3	0.58	(0.49–0.68)	0.66	(0.52–0.85)	0.55	(0.39–0.60)	0.50	(0.35–0.62)	0.47	(0.38–0.52)
Dy_2O_3	5.27	(4.79–5.59)	4.96	(4.23–5.27)	5.10	(4.39–5.58)	5.18	(4.92–5.13)	5.31	(5.11–5.19)
Ho_2O_3	2.68	(2.55–2.91)	2.64	(2.24–2.77)	2.39	(2.09–2.78)	2.33	(2.09–2.43)	2.31	(2.19–2.29)
Er_2O_3	3.04	(2.72–3.19)	3.11	(2.89–3.42)	3.51	(2.98–4.24)	4.22	(4.01–4.18)	3.83	(3.69–3.75)
Tm_2O_3	0.46	(0.24–0.72)	0.44	(0.38–0.61)	0.48	(0.27–0.83)	0.67	(0.52–0.78)	0.33	(0.30–0.34)
Yb_2O_3	2.37	(1.69–3.22)	2.40	(1.76–3.31)	3.38	(1.87–5.07)	4.34	(4.16–4.26)	3.79	(3.48–3.87)
Lu_2O_3	1.26	(1.05–1.50)	1.14	(0.87–1.39)	1.29	(1.01–1.73)	1.42	(1.36–1.38)	1.43	(1.28–1.49)
PbO	0.24	(0.18–0.31)	0.22	(0.06–0.47)	0.26	(0.19–0.31)	0.27	(0.25–0.28)	0.28	(0.24–0.29)
ThO_2	3.12	(2.07–3.39)	2.72	(0.89–4.23)	2.40	(0.78–4.94)	0.68	(0.53–0.79)	2.80	(2.58–2.85)
UO_2	0.37	(0.28–0.58)	0.76	(0.11–3.79)	1.90	(1.26–2.32)	0.02	(0.00–0.04)	1.24	(0.95–1.45)
Tot.	100.39		100.30		100.41		99.58		98.87	
Atoms per formula unit (apfu) calculated on the basis of 4 oxygen atoms										
As	0.764		0.764		0.766		0.408		0.455	
P	0.185		0.192		0.185		0.575		0.500	
Si	0.027		0.025		0.033		0.004		0.032	
V	–		–		–		–		–	
Ca	–		–		–		–		–	
Y	0.739		0.736		0.714		0.757		0.735	
La	–		–		–		–		–	
Ce	0.001		0.002		0.001		–		0.001	
Pr	–		–		–		–		–	
Nd	0.005		0.005		0.005		0.004		0.005	
Sm	0.012		0.010		0.010		0.009		0.007	
Eu	–		–		–		–		–	
Gd	0.038		0.039		0.044		0.025		0.024	
Tb	0.007		0.008		0.007		0.006		0.005	
Dy	0.068		0.064		0.066		0.060		0.064	
Ho	0.034		0.033		0.030		0.026		0.027	
Er	0.028		0.039		0.022		0.048		0.045	
Tm	0.005		0.005		0.006		0.007		0.003	
Yb	0.029		0.029		0.042		0.048		0.043	
Lu	0.015		0.013		0.015		0.015		0.016	
Pb	0.002		0.002		0.002		0.002		0.002	
Th	0.028		0.024		0.022		0.005		0.023	
U	0.003		0.006		0.017		–		0.010	

b.d.l.: below the detection limit

Gasp4. Instead, for all the samples of monazite-(Ce), a combination of equation 1 and equation 2 fully satisfies the pattern shown in Fig. 6b. The P and As contents in the arsenate and phosphate samples, respectively, are always low, as reflected by an average of 1.2(6) mol.% of the phosphate component in gasparite-(Ce) and a maximum 6.60 mol.% of the arsenate component in monazite-(Ce).

Comparison with chemical data reported in the literature

A comparison with the composition of chernovite-(Y) from Mt. Cervandone and that from the Binn Valley, reported by Graeser et al. (1973), shows a P and As content very close to that reported in Table 2 for our samples, resulting in As/(As+P) = 0.76 and 0.84, respectively. A comparison with published chemical analyses of chernovite-(Y) and xenotime-(Y) occurring in different localities (Ondrejka et al., 2007; Förster et al., 2011; Breiter et al., 2009; Li et al., 2019; Alekseev and Marin, 2013; Kerbey, 2013; Mills et al., 2010; Papoutsa and Pe-Piper, 2014) shows that the zircon-type phosphates and arsenates investigated here selectively host HREE, with a very low LREE content. In Fig. 9, the HREE vs. LREE content of several xenotime-(Y) and chernovite-(Y) samples from different geological environments is reported, including crystals from hydrothermally-altered A-type granites, rhyolites, pegmatites (Ondrejka et al., 2007; Breiter et al., 2009; Li et al., 2019; Papoutsa and Pe-Piper, 2014; Förster et al., 2011) and Mn nodules contained in metasedimentary rocks (Mills et al., 2010). From Fig. 9, the majority of the chernovite-(Y)–xenotime-(Y) samples from Mt. Cervandone are mostly enriched in HREE, and only in the outer domains of Ch11 (Ch11_c and Ch11_d) is the fraction of LREE high (reaching

Table 2. (Continued)

	Ch11$_c$		Ch11$_d$		Ch12		Xen14		Mon14	
Wt.%										
As$_2$O$_5$	38.7	(36.5–41.6)	44.23	(43.35–43.35)	38.71	(37.68–40.50)	5.49	(3.45–6.81)	1.95	(1.36–2.84)
P$_2$O$_5$	2.79	(1.17–4.45)	0.27	(0.26–0.27)	4.73	(3.55–5.49)	28.7	(25.99–31.00)	27.71	(26.60–28.55)
SiO$_2$	1.01	(0.43–1.50)	0.03	(0.02–0.05)	0.11	(0.02–0.16)	0.34	(0–0.81)	0.24	(0.02–0.69)
V$_2$O$_5$	b.d.l.		b.d.l.		0.02	(0–0.06)	b.d.l.		b.d.l.	
CaO	0.06	(0.02–0.12)	0.11	(0.10–0.12)	0.01	(0–0.04)	0.01	(0–0.06)	1.19	(0.54–1.59)
Y$_2$O$_3$	28.60	(26.5–31.3)	21.44	(20.05–22.83)	34.84	(34.23–35.51)	39.44	(37.11–41.55)	0.54	(0.39–0.62)
La$_2$O$_3$	0.12	(0.04–0.24)	0.62	(0.52–0.73)	0.05	(0–0.13)	0.03	(0–0.12)	14.18	(12.31–15.82)
Ce$_2$O$_3$	1.24	(0.64–2.34)	3.67	(3.47–3.87)	0.11	(0.01–0.21)	0.07	(0–0.20)	30.84	(28.41–32.95)
Pr$_2$O$_3$	0.28	(0.00–0.63)	1.04	(0.84–1.24)	0.02	(0–0.09)	0.03	(0–0.18)	3.46	(3.09–3.93)
Nd$_2$O$_3$	2.75	(1.38–4.13)	9.91	(8.99–10.82)	0.51	(0.26–0.78)	0.26	(0.08–0.48)	12.88	(12.21–14.46)
Sm$_2$O$_3$	1.79	(1.37–2.14)	5.01	(4.85–5.18)	0.79	(0.52–1.23)	0.73	(0.43–1.04)	2.20	(1.86–2.45)
Eu$_2$O$_3$	b.d.l.		b.d.l.		b.d.l.		b.d.l.		b.d.l.	
Gd$_2$O$_3$	3.24	(2.82–3.57)	5.36	(5.09–5.64)	2.92	(2.52–3.31)	3.84	(2.95–5.03)	1.41	(1.04–2.06)
Tb$_2$O$_3$	0.53	(0.47–0.60)	0.58	(0.57–0.60)	0.78	(0.65–0.97)	0.87	(0.68–1.07)	b.d.l.	
Dy$_2$O$_3$	4.47	(4.19–4.85)	3.05	(2.96–3.14)	5.62	(5.10–6.18)	6.23	(5.36–6.70)	0.27	(0.13–0.43)
Ho$_2$O$_3$	2.6	(2.55–2.63)	2.75	(2.70–2.81)	2.70	(2.25–2.95)	3.27	(2.65–4.14)	0.25	(0.10–0.44)
Er$_2$O$_3$	2.91	(2.63–3.40)	0.97	(0.82–1.12)	2.97	(2.58–3.38)	3.55	(3.13–4.13)	0.03	(0–0.22)
Tm$_2$O$_3$	0.5	(0.42–0.57)	0.47	(0.44–0.51)	0.34	(0.27–0.54)	0.46	(0–0.68)	0.07	(0–0.21)
Yb$_2$O$_3$	2.72	(2.34–3.20)	0.87	(0.83–0.91)	2.11	(1.74–2.43)	3.08	(2.34–3.71)	0.04	(0–0.39)
Lu$_2$O$_3$	0.96	(0.78–1.18)	0.51	(0.49–0.53)	1.23	(0.99–1.54)	1.56	(1.07–1.95)	0.07	(0–0.24)
PbO	0.21	(0.18–0.23)	0.00	(0–0)	0.23	(0.18–0.29)	0.25	(0.04–0.47)	0.03	(0–0.20)
ThO$_2$	2.78	(1.10–4.23)	0.03	(0–0.06)	0.38	(0.21–0.66)	1.89	(0.31–3.87)	2.55	(0.57–5.70)
UO$_2$	1.56	(1.04–2.07)	0.04	(0–0.08)	0.78	(0.60–0.99)	0.40	(0.01–0.74)	0.05	(0–0.17)
Tot.	100.01		100.97		100.08		100.62		100.05	
Atoms per formula unit (apfu) calculated on the basis of 4 oxygen atoms										
As	0.850		0.988		0.817		0.102		0.040	
P	0.098		0.010		0.161		0.861		0.934	
Si	0.042		0.001		0.004		0.012		0.009	
V	–		–		–		–		–	
Ca	0.003		0.005		–		–		0.051	
Y	0.638		0.487		0.748		0.744		0.011	
La	0.002		0.010		–		–		0.208	
Ce	0.019		0.058		0.001		–		0.449	
Pr	0.004		0.016		–		–		0.050	
Nd	0.042		0.151		0.007		0.003		0.183	
Sm	0.026		0.074		0.011		0.008		0.030	
Eu	0.000		–		–		–		–	
Gd	0.045		0.076		0.037		0.039		0.018	
Tb	0.007		0.008		0.01		0.010		–	
Dy	0.060		0.042		0.073		0.071		0.003	
Ho	0.035		0.037		0.034		0.036		0.003	
Er	0.038		0.013		0.003		0.015		–	
Tm	0.007		0.006		0.004		0.005		–	
Yb	0.035		0.011		0.026		0.033		–	
Lu	0.012		0.007		0.015		0.016		–	
Pb	0.002		–		0.002		0.002		–	
Th	0.026		–		0.003		0.015		0.023	
U	0.015		–		0.007		0.003		–	

b.d.l.: below the detection limit

Table 3. Unit-cell parameters of all the samples under investigation.

Sample	Mineral	*a* (Å)	*b* (Å)	*c* (Å)	β (°)	*V* (Å^3)
Ch6	Chernovite-(Y)	7.0030(2)	7.0030(2)	6.2117(3)		304.63(2)
Ch7	Chernovite-(Y)	7.0056(3)	7.0056(3)	6.2307(6)		305.79(3)
Ch8	Chernovite-(Y)	7.0216(3)	7.0216(3)	6.2455(3)		307.92(3)
Ch9	Chernovite-(Y)	7.0176(3)	7.0176(3)	6.2343(4)		307.02(3)
Ch10	Chernovite-(Y)	7.0321(2)	7.0321(2)	6.2552(2)		309.32(2)
Ch11	Chernovite-(Y)–xenotime-(Y) s.s.	6.9591(4)	6.9591(4)	6.1386(7)		297.29(4)
Ch12	Chernovite-(Y)	7.0351(2)	7.0351(2)	6.2630(3)		309.97(2)
Ch13	Chernovite-(Y)	7.0540(3)	7.0540(3)	6.2882(4)		312.89(3)
Ch16	Chernovite-(Y)	7.0648(10)	7.0648(10)	6.2860(12)		313.75(9)
Xen14	Xenotime-(Y)	6.9008(3)	6.9008(3)	6.0447(4)		287.86(3)
Gasp4	Gasparite-(Ce)	6.9259(3)	7.1201(3)	6.7137(3)	104.752(5)	320.16(2)
Gasp3	Gasparite-(Ce)	6.9274(3)	7.1273(3)	6.7118(3)	104.668(3)	320.59(2)
Mon1	Monazite-(Ce)	6.77986(11)	7.00460(12)	6.4587(1)	103.526(2)	298.219(8)
Mon2	Monazite-(Ce)	6.7924(2)	7.0173(2)	6.4735(2)	103.519(3)	300.01(2)
Mon14	Monazite-(Ce)	6.78910(14)	7.01221(12)	6.47346(13)	103.595(2)	299.55(1)

Table 4. A–O and T–O bond distances (in Å), volumes of A- and T-coordination polyhedra (in Å³) and distortion index (DI, calculated using the routine implemented in the software Vesta 3, Momma and Izumi, 2011), based on the structure refinements conducted on all the samples.

Sample	A–O1	A–O1'	A–O2	A–O2'	A–O2''	A–O3	A–O3'	A–O4	A–O4'	T–O1	T–O2	T–O3	T–O4	$V(AO_{8,9})$	$V(TO_4)$	DI(A)	DI(T)
Mon1	2.525(4)	2.452(4)	2.783(4)	2.557(3)	2.642(4)	2.577(3)	2.464(3)	2.519(3)	2.441(3)	1.525(3)	1.546(4)	1.534(3)	1.536(4)	32.29(3)	1.844(10)	0.031	0.004
Mon2	2.510(3)	2.465(3)	2.789(3)	2.559(3)	2.643(2)	2.583(2)	2.469(3)	2.521(2)	2.460(2)	1.536(3)	1.556(3)	1.546(2)	1.523(3)	32.44(2)	1.859(5)	0.031	0.007
Mon14	2.519(3)	2.456(3)	2.791(3)	2.556(3)	2.639(3)	2.581(3)	2.461(3)	2.516(3)	2.449(3)	1.535(2)	1.557(3)	1.549(3)	1.536(4)	32.31(2)	1.875(7)	0.031	0.005
Gasp3	2.550(5)	2.463(5)	2.931(5)	2.532(5)	2.603(5)	2.605(6)	2.435(5)	2.550(5)	2.463(5)	1.668(5)	1.676(5)	1.675(5)	1.660(6)	32.75(6)	2.350(14)	0.037	0.003
Gasp4	2.553(8)	2.449(8)	2.924(7)	2.527(7)	2.618(9)	2.618(9)	2.440(8)	2.546(7)	2.460(7)	1.678(7)	1.660(7)	1.674(7)	1.668(8)	32.80(9)	2.35(1)	0.038	0.004
Ch6	2.4089(13)	2.3019(12)								1.6363(13)				23.45(2)	2.205(5)	0.022	
Ch7	2.414(3)	2.298(3)								1.644(3)				23.46(5)	2.237(14)	0.025	
Ch8	2.419(4)	2.297(4)								1.655(4)				23.51(6)	2.28(2)	0.024	
Ch9	2.410(4)	2.302(3)								1.650(3)				23.46(3)	2.255(11)	0.022	
Ch10	2.419(4)	2.306(3)								1.653(3)				23.66(3)	2.271(8)	0.023	
Ch11	2.401(5)	2.298(5)								1.603(5)				23.27(4)	2.084(10)	0.022	
Ch12	2.416(2)	2.301(3)								1.663(3)				23.55(2)	2.309(4)	0.024	
Ch13	2.424(4)	2.305(5)								1.673(2)				23.71(4)	2.304(11)	0.025	
Ch16	2.422(8)	2.308(9)								1.675(9)				23.73(9)	2.36(2)	0.024	
Xen14	2.389(3)	2.308(3)								1.545(3)				23.22(3)	1.875(7)	0.017	

a maximum of ∼0.39 apfu in Ch11$_d$); also shown by the compositional maps (Fig. 5c,d; Table 2). Thus, a few points of analysis from this study, and those reported by Ondrejka *et al.* (2007) and Förster *et al.* (2011), confirm that, within the A-site of the series chernovite-(Y)–xenotime-(Y), a relatively large fraction of LREE (up to 0.48 apfu) may be hosted, despite being a fairly rare occurrence. As reported in Fig. 8b, evidence of a complex solid solution between the end-members chernovite-(Y), xenotime-(Y) and ThSiO$_4$, according to equation 2, has been reported by several authors (Ondrejka and Uher, 2008; Breiter *et al.*, 2009; Förster *et al.*, 2011; Förster, 2006; Alekseev and Marin, 2013). Chemical data reported by Ondrejka *et al.* (2007) and Förster *et al.* (2011), in particular, show a T-site range composition very close to that reported in the present study. In addition, the heavily altered crystals of Ch13 and Ch16 share similar features with the hydrated chernovite-(Y) and xenotime-(Y) crystals described by Förster (2006) and Förster *et al.* (2011), including a similar Th-content (up to 18.4 wt.% of ThO$_2$), as well as the variable composition, ranging between 9–84 mol.% of the chernovite-(Y) and 0–70 mol.% of xenotime-(Y) component.

The barrel-shaped morphology of gasparite-(Ce), a pseudomorph after synchysite-(Ce), has been emphasised by Graeser and Schwander (1987), and can also be observed for the sample Gasp4 (Fig. 3b). As an alteration product of synchysite-(Ce), gasparite-(Ce) shows rather different chemical features with respect to the three other investigated species crystallised from the hydrothermal fluids. In particular, a comparison with the isostructural monazite-(Ce) highlights an enrichment in Ca and a depletion in Y, probably inherited from the parental REE-carbonate. This present study, similarly to the previous one conducted at Mt. Cervandone by Graeser and Schwander (1987), reports rather narrow compositions, very close to the ideal ones, resulting in a very limited solid solution along the join gasparite-(Ce)–monazite-(Ce). Solid solutions among gasparite-(Ce) and monazite-(Ce) have been described by Ondrejka *et al.* (2007) and Kolitsch and Holtsman (2004a) with As/(As+P) = 0.57–0.64 and 0.89–0.93, respectively, so the wide miscibility gap observed in this study within the monazite-type series is a local feature of the Mt. Cervandone deposit, related possibly to the formation of gasparite-(Ce) after synchysite-(Ce). Conversely, the gasparite-(La), which occurs in the nearby Binn Valley (Vereshchagin *et al.*, 2019), the Swiss flank of Mt. Cervandone, is characterised by a more phosphatian composition with As/(As+P+Si+S) = 0.80.

Crystal structure of the REE phosphates and arsenates

As discussed previously, the tetragonal minerals chernovite-(Y), xenotime-(Y) and thorite are isostructural. Considering the chernovite-(Y)–xenotime-(Y) side of the triangular compositional diagram, the unit-cell volume of the minerals investigated gradually decreases from chernovite-(Y) to xenotime-(Y), as shown by Fig. 10a, which reports the evolution of unit-cell volume (V) *vs.* the As fraction. Similarly, Fig. 10b shows the evolution as a function of As of the tetrahedron volume (calculated using the tools implemented in the software Vesta 3, Momma and Izumi, 2011). For the case of sample Ch11, the unit-cell and structural data, when compared to those of the other chernovite-(Y) samples (see Supplementary Table S16), suggest that the single-crystal investigated (20 μm ×20 μm ×15 μm) belongs to the P-enriched core portion (Ch11$_a$). This assignment is also corroborated by the BSE map shown in Fig. 4d, which suggests that the core portion is the only part able to provide a sufficiently large single crystal. For these reasons, data pertaining to the sample Ch11 have
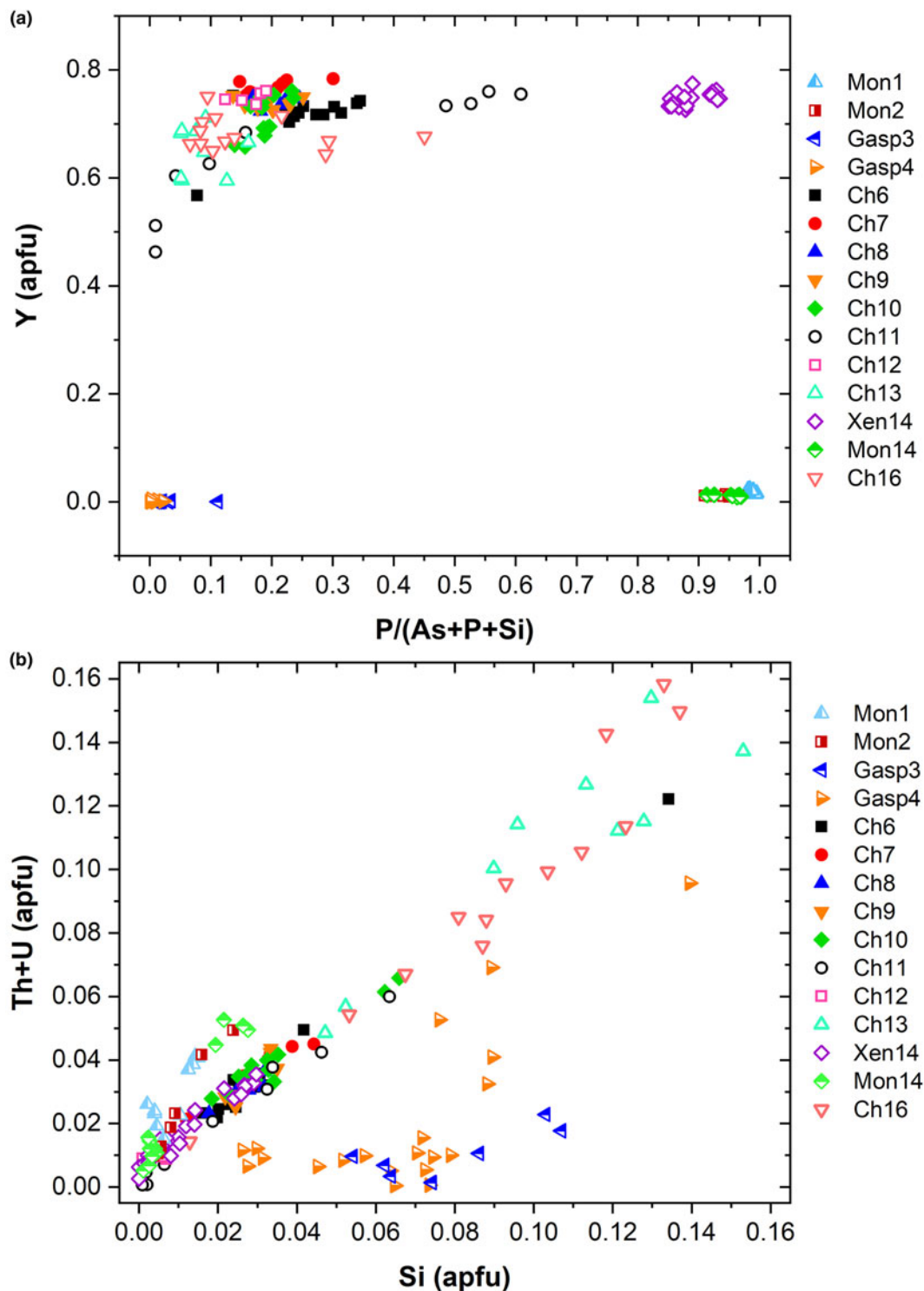
Fig. 6. (a) P/(P+As+Si) *vs.* Y diagram and (b) Si *vs.* Th+U (in apfu) for all the samples under investigation.

been plotted in Fig. 10 assuming the average composition of the core portion reported in Table 2.

Excluding the most Th-enriched samples, all the chernovite-(Y) and xenotime-(Y) samples investigated share an almost identical composition of the REE-bearing *A*-polyhedral site (Supplementary Tables S1–S15), dominated by HREE, which cannot be responsible for the observed variations in the unit-cell and *A*-polyhedron volumes (Fig. 10a; Table 4). Conversely, the cationic population of

the *T*-site affects the volumes of the tetrahedra, with larger values almost linearly correlated with an increase in As and a decrease in P (Fig. 10b). Figures 10c and d show that a strong correlation exists between the tetrahedron volume and both the unit-cell and the *A*-polyhedron volumes, suggesting that the unit-cell volume within this series is controlled significantly by the tetrahedrally-coordinated cations. This is not surprising if we consider the bonding topology of the zircon-type structure, in which any (REE)-polyhedron is
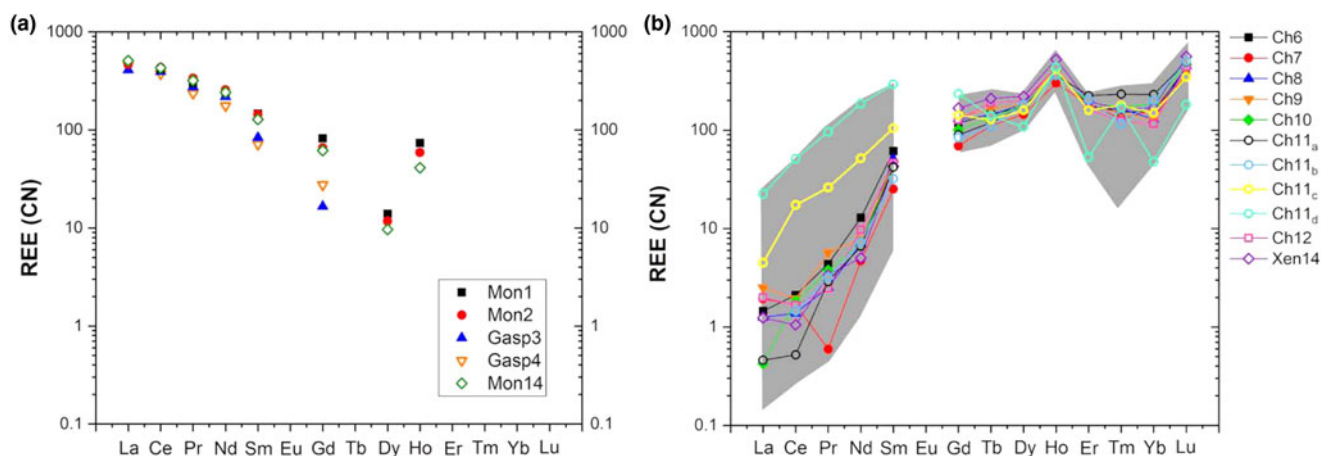
Fig. 7. Average composition of REE (normalised to the CN-1 chondrite, after Wasson and Kallemeyn, 1988) of all the samples of (a) the gasparite-(Ce)–monazite-(Ce) series and (b) the chernovite-(Y)–xenotime-(Y) series. The grey belt in (b) represents the range of the lanthanides composition for all the points of analysis of the chernovite-(Y)-xenotime-(Y) series. Sample Ch11 in (b) is reported as four distinct chemical compositions referring to the core ($Ch11_a$), the interface ($Ch11_b$), the Th-rich rim zone ($Ch11_c$) and the LREE-enriched outer rim zone ($Ch11_d$) (see text, Table 2, Supplementary Table S10 and Figs 4–5 for further details). Elements with concentration < 0.002 apfu are not shown.
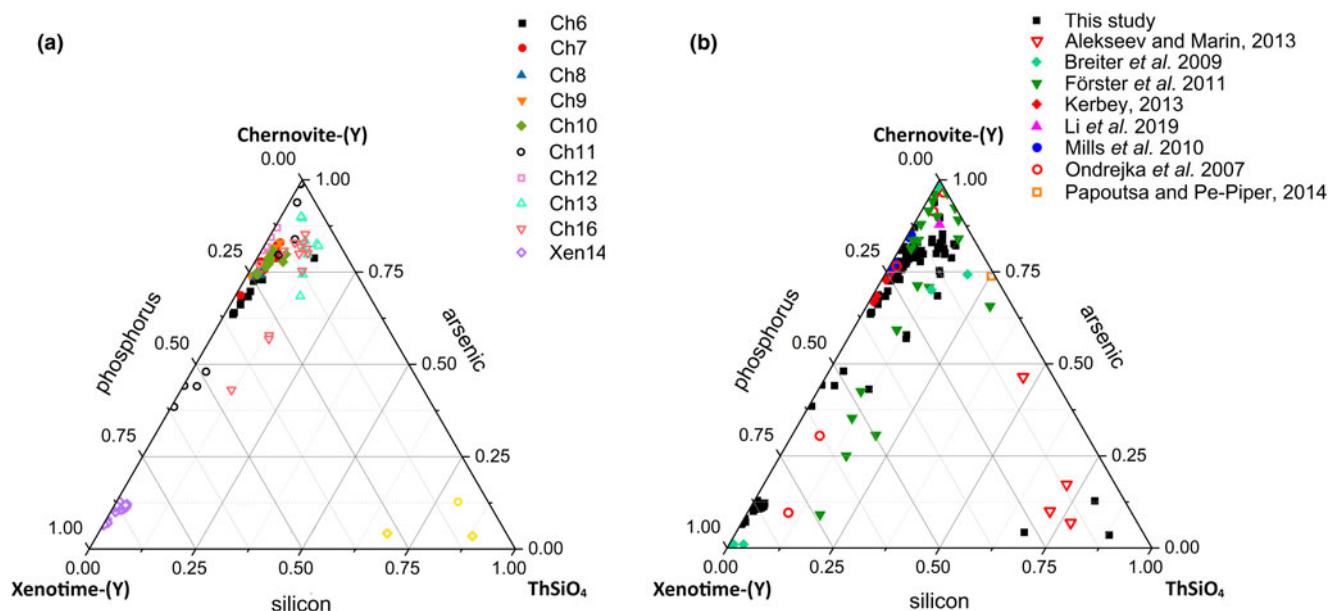
Fig. 8. (a) Triangular chernovite-(Y)–xenotime-(Y)–$ThSiO_4$ compositional diagram, based on the As–P–Si relative abundance, containing all the points of chemical analysis performed on the zircon-type tetragonal minerals. The three points (yellow) close to the $ThSiO_4$ corner represent the $ThSiO_4$ grains found within the Ch11 and Xen14 samples (see also Fig. 4). (b) The same diagram showing the chemical data from this and previously published studies on minerals of the chernovite-(Y)–xenotime-(Y) series.

surrounded by six tetrahedra and, in turn, each tetrahedron share two edges with two adjacent (REE)-polyhedra. As a result, the volumes of the two building units (i.e. polyhedron and tetrahedron) are mutually interconnected. Thus, when the T-site is mostly occupied by the smaller phosphorous, the (REE)-bearing polyhedron adapts with a smaller volume which, in turn, also affects the unit-cell volume; conversely, the opposite trend is observed with an enrichment in arsenic.

A clear deviation from the previously described trends is represented by the Ch13 and Ch16 samples, which show appreciably larger unit-cell volumes, of 312.89(3) $Å^3$ and 313.75(9) $Å^3$, respectively (Fig. 10a). This misalignment is probably related to enrichment in Th and Ca at the A-site, these being elements characterised by larger ionic radii with respect to the HRE (Shannon,

1976), which induce an expansion of the A-polyhedron and, in turn, of the unit-cell volume. A similar behaviour to that described above for the (tetragonal) chernovite-(Y)–xenotime-(Y) series is also shown by the (monoclinic) gasparite-(Ce) and monazite-(Ce). However, in this case, the distribution of the chemical compositions in two clusters close to the ideal end-members prevents a robust extrapolation along the whole series (Fig. 10d).

A correlation among the volumes of (P,As)-tetrahedra and the A-site polyhedra is also shown by the synthetic $REETO_4$ compounds, of which structural models are reported in the Inorganic Crystal Structure Database (Bergerhoff et al., 1987). A comparative analysis of the structural parameters of synthetic REE-bearing phosphates (YPO_4, $LaPO_4$, $CePO_4$, $NdPO_4$, $TbPO_4$, $HoPO_4$, $DyPO_4$, $YbPO_4$

Fig. 9. LREE *vs.* HREE diagram for all the chernovite-(Y)–xenotime-(Y) samples of this study, and for chernovites-(Y), xenotime-(Y) and their solid solutions based on the data from Breiter *et al.* (2009), Ondrejka *et al.* (2007), Mills *et al.* (2010), Förster *et al.* (2011) and Kerbey (2013). Different colours refer to different studies; filled symbols refer to chernovites-(Y), whereas void symbols refer to xenotimes-(Y).
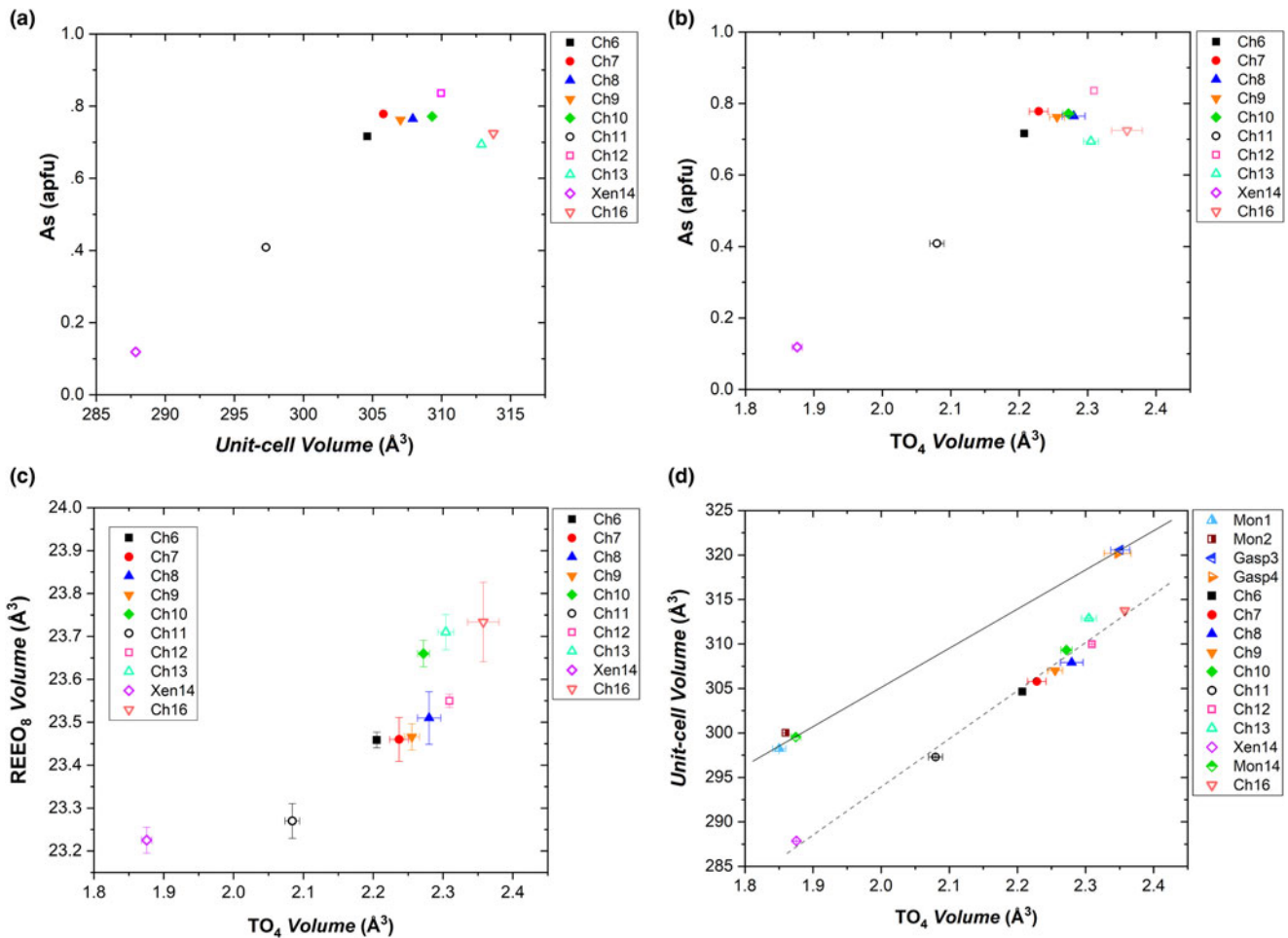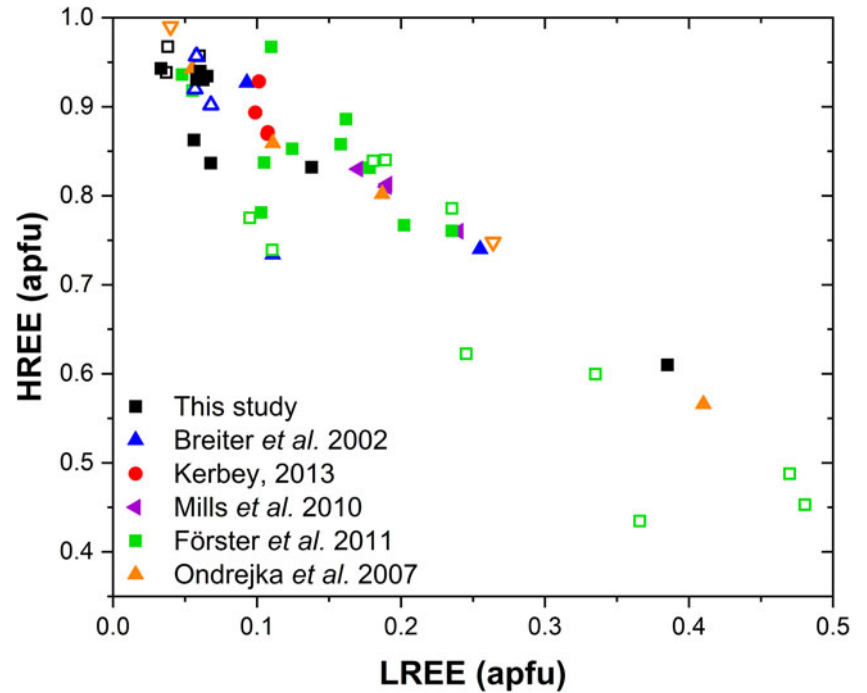

Fig. 10. (a) Unit-cell volume *vs.* As fraction (in apfu), (b) volume of the TO_4 tetrahedron *vs.* As fraction (in apfu) and (c) volume of the TO_4 tetrahedron *vs.* volume of the (REE)-bearing *A*-polyhedron for the samples pertaining to the chernovite-(Y)–xenotime-(Y) series. (d) Volume of the TO_4 tetrahedron *vs.* unit-cell volume for all the samples investigated.

and LuPO$_4$ – Ni *et al.*, 1995) and their As-dominant end-members (YAsO$_4$ – Ledderboge *et al.*, 2018; LaAsO$_4$ – Kang and Schleid, 2005; CeAsO$_4$ – Brahim *et al.*, 2002; NdAsO$_4$ – Schmidt *et al.*, 2005; TbAsO$_4$ – Long and Stager, 1977; HoAsO$_4$ – Schmidt *et al.*, 2005; DyAsO$_4$ – Long and Stager, 1977; YbAsO$_4$ –Kang *et al.*, 2005; and LuAsO$_4$ – Lohmüller *et al.*, 1973) has been carried out. Given the same elemental composition of the REE-bearing A site, the volume of its coordination polyhedron is different in phosphates and arsenates, being always lower in phosphates, pointing out the dominant role played by the TO$_4$ structural units (V$_{TO_4}$ $\approx$ 2.4 Å^3 for AsO$_4$ and $\approx$ 1.8 Å^3 for PO$_4$) in controlling most of the structural features of the REETO$_4$ compounds. Selected structural parameters of synthetic REETO$_4$ compounds are reported in Table S17.

In addition, based on all the structure refinements, the A-polyhedron distortion index (Baur, 1974) has been calculated using the tools implemented in *Vesta 3* (Momma and Izumi, 2011). The A-polyhedron distortion index (DI), following Baur (1974), is based on the measured A–O distances, i.e. DI(A–O), and is expressed as:

$$\text{DI}(A - O) = \frac{1}{8}\left(\sum_{l=1}^{8} |AO_l - AO_{av}|\right)/AO_{av} \qquad (4)$$

for the tetragonal series and

$$\text{DI}(A - O) = \frac{1}{9}\left(\sum_{l=1}^{9} |AO_l - AO_{av}|\right)/AO_{av} \qquad (5)$$

for the monoclinic series, reported in Table 4 (where AO_{av} is the average A–O interatomic distance). The analysis of the calculated distortion index values (Table 4) shows that the increase in As (and decrease in P) leads to an increase in the distortion of the (REE)-site coordination polyhedra in both the tetragonal and monoclinic series.

Concluding remarks

The chemical composition and crystal structure of 15 REE-bearing phosphates and arsenates from the Mt. Cervandone mineral deposit, Western Alps, Italy, have been investigated, using a multi-methodological approach. The REE-pattern of all the analysed samples, shows, as expected, an enrichment in LREE for gasparite-(Ce) and monazite-(Ce), whereas chernovite-(Y) and xenotime-(Y) are characterised by HREE enrichment. Furthermore, a relative enrichment in Ho (when normalised to the CN-1 chondrite composition) has been observed for chernovite-(Y), xenotime-(Y) and monazite-(Ce). Conversely, the two samples of gasparite-(Ce) do not share the same REE-pattern, presumably as gasparite-(Ce) is an alteration product of the carbonate synchysite-(Ce) (Graeser and Schwander, 1987). An almost complete solid solution has been found along the chernovite-(Y) and xenotime-(Y) join, whereas a wide miscibility gap occurs among the investigated end-members of gasparite-(Ce) and monazite-(Ce) series from Mt. Cervandone, probably ascribable to the aforementioned different formation conditions of gasparite-(Ce). On average, chernovite-(Y) and xenotime-(Y) from Mt. Cervandone are characterised by a very selective composition, resulting in a rather low LREE concentration, compared to chemical data available in the literature. Consequently, a limited solid solution occurs between the LREE-bearing monazite-(Ce)

and gasparite-(Ce) and the HREE-bearing xenotime-(Y) and chernovite-(Y). However, the Ch11 sample, showing evidence of reaction, is characterised by a significant enrichment in LREE in its outer rim, suggesting a complex interplay with the circulating hydrothermal fluids. Furthermore, the analysis of the refined structural models reveals the principal role played by the tetrahedrally-coordinated cations in controlling the unit-cell volume and even the REE-polyhedral volume and distortion.

References

Alekseev V.I. and Marin Y.B. (2013) A Tribute to Nicolai Pavlovich Yushkin, one of the discoverers of chernovite. Chernovite-(Y) and other arsenic minerals in rare-metal granites and greisens of the Far East. *Geology of Ore Deposits*, **55**, 601–606.

Andersson S.S. (2019) *Formation of Hydrothermal REE-Phosphate Deposits.* PhD Thesis, Department of Geosciences and Geography **A76**, Helsinki.

Anthony J.W., Bideaux R.A., Bladh K.W. and Nichols M.C. (2000) *Handbook of Mineralogy, IV, Phosphates, Arsenates, Vanadates.* Mineral Data Publishing, Tucson, Arizona, USA

Balaram V. (2019) Rare earth elements: A review of applications, occurrence, exploration, analysis, recycling, and environmental impact. *Geoscience Frontiers*, **10**, 1285–1303.

Baur W.H. (1974) The geometry of polyhedral distortions. Predictive relationships for the phosphate group. *Acta Crystallographica*, **B30**, 1195–1215.

Beall G.W., Boatner L.A., Mullica D.F. and Milligan W.O. (1981) The structure of cerium orthophosphate, a synthetic analogue of monazite. *Journal of Inorganic and Nuclear Chemistry*, **43**, 101–105.

Bergerhoff G., Brown I.D. and Allen F. (1987) Crystallographic databases. *International Union of Crystallography, Chester*, **360**, 77–95.

Blengini G.A., Mathieux F., Mancini L., Nyberg M. and Viegas H.M. (2020) *Study on the EU's list of Critical Raw Materials. Executive Summary.* Publication Office of the European Commission, Luxembourg.

Boatner L.A. (2002) Synthesis, structure, and properties of monazite, pretulite, and xenotime. Pp. 87–121 in: *Phosphates: Geochemical, Geobiological and Materials Importance* (M.J. Kohn, J. Rakovan and J.M. Hughes, editors). Reviews in Mineralogy and Geochemistry, **48**. Mineralogical Society of America and the Geochemical Society, Chantilly, Viginia, USA.

Brahim A., Mohamed Mongi F. and Amor H. (2002) Cerium arsenate, CeAsO$_4$. *Acta Crystallographica*, **E58**, i98–i99.

Breiter K., Čopjaková R. and Škoda R. (2009) The involvement of F, CO$_2$, and As in the alteration of Zr–Th–REE-bearing accessory minerals in the Hora Svaté Kateřiny A-type granite, Czech Republic. *The Canadian Mineralogist*, **47**, 1375–1398.

Cabella R., Lucchetti G. and Marescotti P. (1999) Occurrence of LREE-and Y-arsenates from a Fe-Mn deposit, Ligurian Briançonnais Domain, Maritime Alps, Italy. *The Canadian Mineralogist*, **37**, 961–972.

Černý P. (1991a) Rare-element granitic pegmatites. Part I: anatomy and internal evolution of pegmatitic deposits. *Geoscience Canada*, **18**, 49–67.

Černý P. (1991b) Rare-element granitic pegmatites. Part II: Regional to global environments and petrogenesis. *Geoscience Canada*, **18**, 68–81.

Černý P. and Ercit T.S. (2005) The classification of granitic pegmatites revisited. *The Canadian Mineralogist*, **43**, 2005–2026.

Cesbron F.P. (1989) Mineralogy of the rare-earth elements. Pp. 3–26. In *Lanthanides, Tantalum and Niobium* (P. Möller, P. Černý and F. Saupé, editors). Springer, Berlin, Heidelberg, Germany.

Cheng Z., Zhang Z., Aibai A., Kong W. and Holtz F. (2018) The role of magmatic and post-magmatic hydrothermal processes on rare-earth element mineralization: A study of the Bachu carbonatites from the Tarim Large Igneous Province, NW China. *Lithos*, 314, 71–87.

Clavier N., Podor R. and Dacheux N. (2011) Crystal chemistry of the monazite structure. *Journal of the European Ceramic Society*, 31, 941–976.

Connelly N.G., Damhus T., Hartshorn R.M. and Hutton A.T. (2005) *Nomenclature of inorganic chemistry: IUPAC recommendations 2005. The red book*. Royal Society of Chemistry, Cambridge, UK.

Čopjaková R., Novák M. and Franců E. (2011) Formation of authigenic monazite-(Ce) to monazite-(Nd) from Upper Carboniferous graywackes of the Drahany Upland: Roles of the chemical composition of host rock and burial temperature. *Lithos*, 127, 373–385.

Dal Piaz G. (1975) Angelo Bianchi. La val Devero ed i suoi minerali. *Memorie Istituto Geologia Università Padova*, allegato volume X. Società Cooperativa Tipografica, Padova, Italy.

Della Ventura G., Mottana A., Parodi G., Raudsepp M., Bellatreccia F., Caprilli E., Rossi P. and Fiori S. (1996) Monazite-huttonite solid-solutions from the Vico Volcanic Complex, Latium, Italy. *Mineralogical Magazine*, 60, 751–758.

Demartin F., Pilati T., Diella V., Donzelli S. and Gramaccioli C.M. (1991) Alpine monazite; further data. *The Canadian Mineralogist*, 29, 61–67.

Ercit T.S., Linnen R.L. and Samson I.M. (2005) REE-enriched granitic pegmatites. Pp. 175–199 in: *Rare-Element Geochemistry and Mineral Deposits*. Geological Association of Canada, GAC Short Course Notes, 17.

Fleischer M. and Altschuler Z.S. (1969) The relationship of the rare-earth composition of minerals to geological environment. *Geochimica et Cosmochimica Acta*, 33, 725–732.

Förster H.J. (2006) Composition and origin of intermediate solid solutions in the system thorite–xenotime–zircon–coffinite. *Lithos*, 88, 35–55.

Förster H.J., Ondrejka M. and Uher P. (2011) Mineralogical responses to subsolidus alteration of granitic rocks by oxidizing As-bearing fluids: REE arsenates and As-rich silicates from the Zinnwald granite, eastern Erzgebirge, Germany. *The Canadian Mineralogist*, 49, 913–930.

Gatta G.D., Rotiroti N., Cámara F. and Meven M. (2018) On the labyrinthine world of arsenites: a single-crystal neutron and X-ray diffraction study of cafarsite. *Physics and Chemistry of Minerals*, 45, 819–829.

Gatta G.D., Milani S., Corti L., Comboni D., Lotti P., Merlini M. and Liermann H-P. (2019) Allanite at high pressure: effect or REE on the elastic behaviour of epidote-group minerals. *Physics and Chemistry of Minerals*, 46, 783–793.

Gatta G.D., Pagliaro F., Lotti P., Guastoni A., Cañadillas-Delgado L., Fabelo O. and Gigli L. (2021) Allanite at high temperature: effect of REE on the thermal behaviour of epidote-group minerals. *Physics and Chemistry of Minerals*, 48, 1–16.

Goldin B.A., Yushkin N.P. and Fishman M.V. (1967) A new yttrium mineral, chernovite. *Zapiski Vsesoyuznogo Mineralogicheskogo Obshchestva*, 96, 699–704.

Graeser S. and Albertini C. (1995) Wannigletscher und Conca Cervandone. *Lapis*, 20, 52–56.

Graeser S. and Schwander H. (1987) Gasparite-(Ce) and monazite-(Nd): two new minerals to the monazite group from the Alps. *Schweizerische Mineralogische und Petrographische Mitteilungen*, 67, 103–113.

Graeser S., Schwander H. and Stalder H.A. (1973) A solid solution series between xenotime (YtPO₄) and chernovite (YtAsO₄). *Mineralogical Magazine*, 39, 145–151.

Guastoni A., Pezzotta F. and Vignola P. (2006) Characterization and genetic inferences of arsenates, sulfates and vanadates of Fe, Cu, Pb, Zn from Mt. Cervandone (Western Alps, Italy). *Periodico di Mineralogia*, 75, 141–150.

Guastoni A., Pozzi G., Secco L., Schiazza M., Pennacchioni G., Fioretti A. and Nestola F. (2016) Monazite-(Ce) and xenotime-(Y) from an LCT, NYF teritary pegmatite field: evidence from a regional study in the Central Alps (Italy and Switzerland). *The Canadian Mineralogist*, 54, 863–877.

Harlov D.E. and Förster H.-J. (2002) High-grade fluid metasomatism on both a local and regional scale: The Seward Peninsula, Alaska and the Val Strona di Omegna, Ivrea-Verbano zone, northern Italy. Part II: Phosphate mineral chemistry. *Journal of Petrology*, 43, 801–824.

Harlov D.E., Förster H-J. and Nijland T.G. (2002) Fluid induced nucleation of (Y + REE)-phosphate minerals in apatite: nature and experiment Part I. chlorapatite. *American Mineralogist*, 87, 245–261

Harlov D.E., Wirth R. and Hetherington C.J. (2007) The relative stability of monazite and huttonite at 300–900° C and 200–1000 MPa: Metasomatism and the propagation of metastable mineral phases. *American Mineralogist*, 92, 1652–1664.

Johan Z. and Johan V. (2005) Accessory minerals of the Cínovec (Zinnwald) granite cupola, Czech Republic: indicators of petrogenetic evolution. *Mineralogy and Petrology*, 83, 1131–50.

Kang D.H. and Schleid T. (2005) Einkristalle von La[AsO₄] im Monazit-und Sm[AsO₄] im Xenotim-Typ. *Zeitschrift für anorganische und allgemeine Chemie*, 631, 1799–1802.

Kang D.H., Höss P. and Schleid T. (2005) Xenotime-type Yb[AsO₄]. *Acta Crystallographica*, E61, i270–i272.

Kerbey H.C. (2013) Chernovite-(Y) in reduction spots in Welsh Slate. *Journal of the Russell Society*, 16, 60–63.

Kolitsch U. and Holtstam D. (2004a) Crystal chemistry of REEXO4 compounds (X = P, As, V). I. Paragenesis and crystal structure of phosphatian gasparite-(Ce) from the Kesebol Mn-Fe-Cu deposit, Västra Götaland, Sweden. *European Journal of Mineralogy*, 16, 111–116.

Kolitsch U. and Holtstam D. (2004b) Crystal chemistry of REEXO₄ compounds (X = P, As, V). II. Review of REEXO₄ compounds and their stability fields. *European Journal of Mineralogy*, 16, 117–126.

Ledderboge F., Nowak J., Massonne H.J., Förg K., Höppe H.A. and Schleid T. (2018) High-pressure investigations of yttrium (III) oxoarsenate (V): Crystal structure and luminescence properties of Eu³⁺-doped scheelite-type Y[AsO₄] from xenotime-type precursors. *Journal of Solid State Chemistry*, 263, 65–71.

Li M.Y.H., Zhou M.F. and Williams-Jones A.E. (2019) The genesis of regolith-hosted heavy rare earth element deposits: Insights from the world-class Zudong deposit in Jiangxi Province, South China. *Economic Geology*, 114, 541–568.

Lohmüller V.G., Schmidt G., Deppisch B., Gramlich V. and Scheringer C. (1973) The crystal structures of yttrium vanadate, lutetium phosphate and lutetium arsenate. *Acta Crystallographica*, B29, 141–142.

Long F.G. and Stager C.V. (1977) Low temperature crystal structure of TbAsO₄ and DyAsO₄. *Canadian Journal of Physics*, 55, 1633–1640.

Long K.R., Van Gosen B.S., Foley N.K. and Cordier D. (2012) The principal rare earth elements deposits of the United States: A summary of domestic deposits and a global perspective. Pp. 131–155 in: *Non-Renewable Resource Issues* (Sinding-Larsen, R. and Wellmer, F.W., editors) Springer, Dordrecht, The Netherlands.

Mancheri N.A. (2015) World trade in rare earths, Chinese export restrictions, and implications. *Resources Policy*, 46, 262–271.

Mancini S. (2000) *Le Mineralizzazioni a Manganese Delle Alpi Apuane*. PhD dissertation, University of Pisa, Italy.

Mazeina L., Ushakov S.V., Navrotsky A. and Boatner L.A. (2005) Formation enthalpy of ThSiO₄ and enthalpy of the thorite→ huttonite phase transition. *Geochimica et Cosmochimica Acta*, 69, 4675–4683.

Mesbah A., Clavier N., Lozano-Rodriguez M.J., Szenknect S. and Dacheux N. (2016) incorporation of thorium in the zircon structure type through the Th₁₋ₓErₓ(SiO₄)₁₋ₓ(PO₄)ₓ thorite–xenotime solid solution. *Inorganic Chemistry*, 55, 11273–11282.

Migdisov A., Guo X., Nisbet H., Xu H. and Williams-Jones A.E. (2019) Fractionation of REE, U, and Th in natural ore-forming hydrothermal systems: Thermodynamic modeling. *The Journal of Chemical Thermodynamics*, 128, 305–319.

Mills S.J., Kartashov P.M., Kampf A.R. and Raudsepp M. (2010) Arsenoflorencite-(La), a new mineral from the Komi Republic, Russian Federation: description and crystal structure. *European Journal of Mineralogy*, 22, 613–621.

Momma K. and Izumi F. (2011) VESTA 3 for three-dimensional visualization of crystal, volumetric and morphology data. *Journal of Applied Crystallography*, 44, 1272–1276.

Mooney R.C. (1948) Crystal structures of a series of rare earth phosphates. *The Journal of Chemical Physics*, 16, 1003–1003.

Ni Y., Hughes J.M. and Mariano A.N. (1995) Crystal chemistry of the monazite and xenotime structures. *American Mineralogist*, 80, 21–26.

Ondrejka M. and Uher P. (2008) Accessory (REE+Y)XO$_4$ phases: substitutions of As, S, Nb, Zr, Th, Ca and Sr in endogenous systems. *Geochimica et Cosmochimica Acta*, **72**(12), Supplement 706 [Goldschmidt Conference Abstracts]

Ondrejka M., Uher P., Pršek J. and Ozdín D. (2007) Arsenian monazite-(Ce) and xenotime-(Y), REE arsenates and carbonates from the Tisovec-Rejkovo rhyolite, Western Carpathians, Slovakia: Composition and substitutions in the (REE, Y)XO$_4$ system (X = P, As, Si, Nb, S). *Lithos*, **95**, 116–129.

Papoutsa A. and Pe-Piper G. (2014) Variation of REE-hydrothermal circulation in complex shear zones: The Cobequid Highlands, Nova Scotia. *The Canadian Mineralogist*, **52**, 943–968.

Petříček V., Dušek M. and Palatinus L. (2014) Crystallographic computing system JANA2006: general features, *Zeitschrift für Kristallographie*, **229**, 345–352.

Richter L., Diamond L.W., Atanasova P., Banks D.A. and Gutzmer J. (2018) Hydrothermal formation of heavy rare earth element (HREE)–xenotime deposits at 100° C in a sedimentary basin. *Geology*, **46**, 263–266.

Rigaku Oxford Diffraction (2019) *CrysAlisPro Software system, version 1.171.40.67a.* Rigaku Corporation, Wroclaw, Poland.

Rosenblum S. and Fleischer M. (1995) *The Distribution of Rare-Earth Elements in Minerals of the Monazite Family.* US Geological Survey Bulletin 2140. US Government Printing Office, Washington, 70 pp.

Schmidt M., Müller U., Cardoso G.R., Milke E. and Binnewies M. (2005) Zum chemischen Transport und zur Kristallstruktur von Seltenerdarsenaten (V). *Zeitschrift für anorganische und allgemeine Chemie*, **631**, 1154–1162.

Sengupta D. and Van Gosen B.S. (2016) Placer-type rare earth element deposits. Pp. 81–100 in: *Rare Earth and Critical Elements in Ore Deposits* (P.L. Verplanckand and M.W. Hitzman, editors). Reviews in Economic Geology, **18**. Society of Economic Geologists, Littleton, Colorado, USA.

Seydoux A.M. and Montel J.M. (1997) Experimental determination of the thorite-huttonite phase transition. *Terra Nova*, **9**, 421 [Abstract Supplements No. 1].

Shannon R.D. (1976) Revised effective ionic radii and systematic studies of interatomic distances in halides and chalcogenides. *Acta Crystallographica*, **A32**, 751–767.

Spear F.S. and Pyle J.M. (2002) Apatite, monazite, and xenotime in metamorphic rocks, Pp. 293–335. In: *Phosphates: Geochemical, Geobiological, and Materials Importance* (M.J. Kohn, J. Rakovan and J.M. Hughes, editors). Reviews in Mineralogy and Geochemistry, **48**. Mineralogical Society of America and the Geochemical Society, Washington DC.

Speer J.A. and Cooper B.J. (1982) Crystal structure of synthetic hafnon, HfSiO$_4$, comparison with zircon and the actinide orthosilicates. *American Mineralogist*, **67**, 804–808.

Strada M. and Schwendimann G. (1934) La struttura cristallina di alcuni fosfati ed arseniati di metalli trivalenti. II. Arseniato e fosfato di yttrio. *Gazzetta Chimica Italiana*, **64**, 662–674.

Strzelecki A.C., Barral T., Estevenon P., Mesbah A., Goncharov V., Baker J., Bai J., Clavier N., Szenknect S., Migdisov A., Xu H., Ewing R.C., Dacheux N. and Guo X. (2021) The role of water and hydroxyl groups in the structures of stetindite and coffinite, MSiO$_4$ (M = Ce, U). *Inorganic Chemistry*, **60**, 718–735.

U.S. Geological Survey (2011) *2009 Rare Earth. Minerals Yearbook 2009.* U.S. Geological Survey, Reston, Virginia, USA.

U.S. Geological Survey (2021) *Mineral Commodity Summaries 2021.* U.S. Geological Survey, Reston, Virginia, USA.

Ushakov S.V., Helean K.B., Navrotsky A. and Boatner L.A. (2001) Thermochemistry of rare-earth orthophosphates. *Journal of Materials Research*, **16**, 2623–2633.

Vereshchagin O.S., Britvin S.N., Perova E.N., Brusnitsyn A.I., Polekhovsky Y.S., Shilovskikh V.V., Bocharov V.N., van der Burgt A., Cuchet S. and Meisser N. (2019) Gasparite-(La), La(AsO$_4$), a new mineral from Mn ores of the Ushkatyn-III deposit, Central Kazakhstan, and metamorphic rocks of the Wanni glacier, Switzerland. *American Mineralogist*, **104**, 1469–1480.

Voncken J.H.L. (2016) *The Rare Earth Elements: An Introduction.* Springer, Berlin.

Warr L.N. (2021) IMA–CNMNC approved mineral symbols. *Mineralogical Magazine*, **85**, 291–320.

Wasson J.T. and Kallemeyn G.W. (1988) Compositions of chondrites. *Philosophical Transactions of the Royal Society of London*, **A325**, 535–544.

Zepf V. (2013) Rare Earth Elements: What and where they are. Pp. 11–39 in: *Rare Earth Elements*. Springer, Berlin, Heidelberg.